Journal Pre-proofs

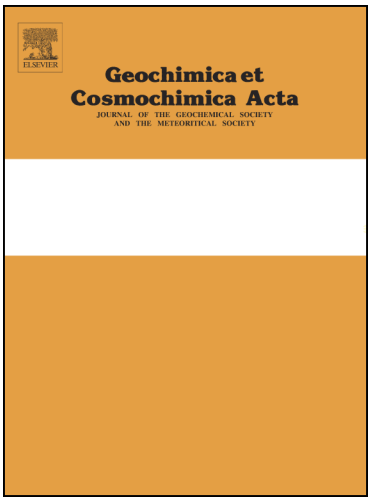

Abiotic methane generation through reduction of serpentinite-hosted dolomite: implications for carbon mobility in subduction zones

Weigang Peng, Lifei Zhang, Simone Tumiati, Alberto Vitale Brovarone, Han Hu, Yachun Cai, Tingting Shen

PII: S0016-7037(21)00451-8
DOI: https://doi.org/10.1016/j.gca.2021.07.033
Reference: GCA 12317

To appear in: *Geochimica et Cosmochimica Acta*

Received Date: 18 February 2021
Revised Date: 17 July 2021
Accepted Date: 27 July 2021

Please cite this article as: Peng, W., Zhang, L., Tumiati, S., Vitale Brovarone, A., Hu, H., Cai, Y., Shen, T., Abiotic methane generation through reduction of serpentinite-hosted dolomite: implications for carbon mobility in subduction zones, *Geochimica et Cosmochimica Acta* (2021), doi: https://doi.org/10.1016/j.gca.2021.07.033

Abiotic methane generation through reduction of serpentinite-hosted dolomite: implications for carbon mobility in subduction zones

Weigang Peng[a,b,c], Lifei Zhang[a,*], Simone Tumiati[c],

Alberto Vitale Brovarone[d,e], Han Hu[a], Yachun Cai[b], Tingting Shen[f]

[a] *MOE Key Laboratory of Orogenic Belts and Crustal Evolution, School of Earth and Space Sciences, Peking University, Beijing 100871, China*

[b] *Deep Sea Research Center, Pilot National Laboratory for Marine Science and Technology (Qingdao), Qingdao 266061, China*

[c] *Dipartimento di Scienze della Terra, Università degli Studi di Milano, via Mangiagalli 34, 20133 Milano, Italy*

[d] *Dipartimento di Scienze Biologiche, Geologiche e Ambientali, Alma Mater Studiorum Università di Bologna, Piazza di Porta San Donato 1, 40126 Bologna, Italy*

[e] *Sorbonne Université, Muséum National d'Histoire Naturelle, UMR CNRS 7590, IRD, Institut de Minéralogie, de Physique des Matériaux et de Cosmochimie, IMPMC, 4 Place Jussieu, 75005 Paris, France*

[f] *Institute of Geology, Chinese Academy of Geological Sciences, Beijing 100037, China*

*Corresponding author: Lifei Zhang

E-mail: lfzhang@pku.edu.cn

Telephone: +86-010-62751145

ABSTRACT

Abiotic methane has been increasingly detected at the surface of Earth and other terrestrial planets, exerting a strong effect on the study of chemolithoautotrophic life and thus astrobiology. In contrast, abiotic methane generation in subduction zones, which is intimately linked to questions such as the mechanisms of deep carbon mobility, has received scarce attention. Experiments elucidated the significant production of abiotic methane through reduction of carbonate minerals under subduction zone conditions, whereas detailed geological conditions and processes for the reduction in natural rocks are hitherto poorly understood. Here, we report carbonate reduction and genesis of abiotic methane in dolomitized serpentinites (referred to as ophidolomites) from a fossil subduction zone (SW Tianshan, China). Detailed petrological, Raman spectroscopic, strontium and carbon isotopic, and thermodynamic results provide evidence for dolomite reduction into the phase assemblage of calcite + brucite + methane, likely associated with retrograde serpentinization starting at 7−9 kbar and 410−430 ^{o}C in the subduction zone. Microthermometric data for dolomite-hosted fluid inclusions are consistent with petrographic observations, indicative of fluid entrapment postdating the onset of dolomite reduction during exhumation. Model calculations suggest that water-rich fluids characterized by relatively high hydrogen fugacities can create favorable conditions for the reduction process, which, however, do not exclude the possibility of carbonate methanation by hydrogen-rich fluids as reported in previous studies. The widespread occurrence

of methane in these rocks gives credence to the intricate redox transformations of subducted carbon, implying that the elevated hydrogen fugacities may facilitate abiotic synthesis of methane through dolomite reduction at convergent plate boundaries. Our work shows that alteration of dolomite-bearing lithologies represents a potential source for abiotic methane in subduction zones, which may have implications for the transfer of subducted carbon.

Keywords: Abiotic methane; Dolomite reduction; Ophicarbonate; Hydrogen fugacity; Subduction zone; Chinese southwestern Tianshan

1. INTRODUCTION

Redox transformations in subduction zones regulate the valence of carbon (C), and thus control the long-term fate of subducted C (e.g., Hayes and Waldbauer, 2006; Evans, 2012; Galvez and Pubellier, 2019; Tumiati and Malaspina, 2019; Sheik et al., 2020). Carbonation of subduction-zone rocks at forearc to subarc depths by interactions with slab-derived carbon dioxide (CO_2)-bearing fluids gives insights into C sequestration under oxidized conditions (Tumiati et al., 2013; Piccoli et al., 2016, 2018; Scambelluri et al., 2016; Jaeckel et al., 2018; Sieber et al., 2018, 2020; Peng et al., 2020; Hu et al., 2021). On the other hand, reduction of carbonate minerals at convergent plate boundaries generates graphite and/or hydrocarbons such as methane (CH_4), modulating the distribution of subducted C between solid and fluid inventories (Malvoisin et al.,

2012; Galvez et al., 2013a, b; Vitale Brovarone et al., 2017; Tao et al., 2018a; Giuntoli et al., 2020). Graphite formation through carbonate reduction during shallow subduction offers a potential mechanism to retain C in subducted slabs, which may facilitate C transport into the deep Earth (Malvoisin et al., 2012; Galvez et al., 2013a, b). In contrast, the release of CH_4 from subducted ophicalcites (Western Alps, Italy; Vitale Brovarone et al., 2017; Giuntoli et al., 2020) and carbonated eclogites (SW Tianshan, China; Tao et al., 2018a), attributed to hydrogen (H_2)-induced reduction of calcite (referred to as carbonate methanation; Etiope and Sherwood Lollar, 2013 and references therein) and aqueous reduction of ferroan dolomite, respectively, provides evidences for mobile deep C reservoirs. Moreover, olivine-hosted secondary CH_4-bearing fluid inclusions were observed in partially serpentinized rocks within and above subducted slabs, interpreted as being due to the reduction of C-bearing species in metamorphic fluids through subduction-zone serpentinization (Sachan et al., 2007; Vitale Brovarone et al., 2020; Boutier et al., 2021). Therefore, investigating mechanisms for abiotic CH_4 generation in subduction zones is helpful to our comprehension of the transfer of slab C.

Abiotic CH_4 has been increasingly identified during the past decades, particularly at shallow geodynamic settings (such as in mid-ocean ridge hydrothermal systems; e.g., Kelley et al., 2001, 2005), revealing its more extensive distribution than conventionally assumed (Etiope and Sherwood Lollar, 2013; Etiope and Schoell, 2014). In submarine environments, the hydration of

exposed mantle rocks (referred to as serpentinization) commonly accompanies H_2 discharge, which may favor the synthesis of abiotic CH_4—with or without other short-chain hydrocarbons, such as ethane (C_2H_6), propane (C_3H_8), and butane (C_4H_{10})—via Fischer−Tropsch-type reduction of aqueous CO_2 in seawater (e.g., Charlou et al., 2002, 2010; Proskurowski et al., 2008). Conversely, several metastable intermediate species (e.g., formates), instead of light hydrocarbons, have been considered to be predominantly generated by abiotic reduction of dissolved inorganic C during seawater circulation through ultramafic rocks in the subsurface (McCollom et al., 2001; McDermott et al., 2015). Geological production of these organic compounds plays a potential role in the origin of chemolithoautotrophic life on Earth and other terrestrial planets (e.g., McCollom and Seewald, 2013; McDermott et al., 2015; Ménez, 2020; Truche et al., 2020). Furthermore, H_2-induced reduction of C-bearing species by serpentinization within olivine-hosted fluid inclusions in submarine and subaerial vent systems likely represents a widespread reservoir of abiotic CH_4 over geological timescales (Klein et al., 2019; Grozeva et al., 2020). In contrast, abiotic formation of CH_4 in subduction zones, which is closely related to the mechanisms of deep C mobility, has received scarce attention. Experiments demonstrated that abiotic CH_4 can be generated under subduction zone conditions through reduction of subducted C (e.g., carbonate minerals, organic matter, and dissolved aqueous organic species; Sharma et al., 2009; Lazar et al., 2014; Huang et al., 2017; Li, 2017; Mukhina et al., 2017; Tao et al., 2018a). However, the manifestations of abiotic CH_4 in natural

subduction-zone rocks, as well as the geological conditions and reaction pathways for its production, have been paid insufficient attention, even though CH_4-bearing fluid inclusions are not particularly rare in metamorphic lithologies within and above subducted slabs (Shi et al., 2005; Sachan et al., 2007; Song et al., 2009; Arai et al., 2012; Vitale Brovarone et al., 2017, 2020; Tao et al., 2018a; Giuntoli et al., 2020; Boutier et al., 2021; Zhang et al., 2021).

In this contribution, we report dolomite reduction and genesis of abiotic CH_4 in ophidolomites belonging to the ultramafic unit of Changawuzi in the Chinese southwestern Tianshan high-pressure–ultrahigh-pressure (H*P*–UH*P*) metamorphic belt. We show and discuss petrology, Raman spectroscopy, microthermometry, strontium (Sr) and C isotope geochemistry, and thermodynamic modelling to improve understanding of abiotic CH_4 generation in subduction zones.

2. GEOLOGICAL BACKGROUND AND SAMPLES

The Chinese southwestern Tianshan H*P*–UH*P* metamorphic belt is located in the northwest of China and formed due to northward subduction of the Tarim Plate underneath the Yili–Central Tianshan Plate (Fig. 1A; Zhang et al., 2013). The spatial distribution of H*P*–UH*P* rocks in this metamorphic belt allows the subdivision of a southern H*P* sub-belt and a northern, coesite-bearing, UH*P* sub-belt (Fig. 1B; Lü and Zhang, 2012; Lü et al., 2012a, b; Zhang et al., 2013). The current work focuses on the Chinese southwestern Tianshan UH*P* metamorphic

belt, which mainly experienced (1) UH*P* metamorphism (~30 kbar and ~500 °C) at ca. 320 Ma, (2) peak temperature metamorphism at H*P* conditions during exhumation (i.e., thermal relaxation; ~22 kbar and ~600 °C) at ca. 310–315 Ma, and (3) multistage exhumation to relatively shallow depths (from eclogite facies to greenschist facies) (Tan et al., 2017; Zhang et al., 2019 and references therein).

The main rock types in the Chinese southwestern Tianshan H*P*–UH*P* metamorphic belt are garnet–phengite schists, marbles, blueschists, eclogites, and serpentinites with associated rodingites (e.g., Shen et al., 2015). Serpentinites are mostly exposed at Changawuzi in an area of about 6–10 km^2 (Fig. 1C), recording two stages of serpentinization: (1) a seawater-related hydration process of oceanic mantle rocks overprinted by the UH*P* metamorphism (37 ± 7 kbar and 520 ± 10 °C) during subduction (Shen et al., 2015) and (2) a later rehydration process of metamorphic and/or primary olivine and pyroxene during exhumation (i.e., retrograde serpentinization) starting at 7–9 kbar and 410–430 °C and propagating to lower *P*–*T* conditions (Li et al., 2007, 2010). Carbonated serpentinites, including H*P* ophidolomites and low-pressure (L*P*) ophimagnesites and listvenites, occur in association with the serpentinites and record two carbonation processes that happened at different stages of exhumation from a depth of ~70 km to relatively shallow crustal levels (Peng et al., 2020).

The herein studied CH_4-bearing ophidolomites are intimately associated with (carbonated) serpentinites in the Changawuzi ultramafic blocks (Fig. 1C), which are surrounded by mica schists (for detailed field occurrence, see Peng et al.,

2020). These ophidolomites are characterized by discontinuous and folded dolomite veins hosted in serpentinites, in which dolomite is encircled by yellowish calcite and brucite (Fig. 2A and B). Other than the studied samples at Changawuzi, CH_4-bearing fluid inclusions were also reported in carbonated eclogites in adjacent localities of Kebuerte and Habutengsu (Fig. 1B; Tao et al., 2018a), indicating a relatively widespread distribution of CH_4 in the Chinese southwestern Tianshan H*P*–UH*P* metamorphic belt.

3. METHODS

3.1. Scanning electron microscopic analyses

Back-scattered electron (BSE) images and compositional X-ray maps were obtained using an FEI Quanta 650 FEG scanning electron microscope (SEM) equipped with an Oxford INCA X-MAX50 250+ energy dispersive X-ray spectrometer at the School of Earth and Space Sciences (SESS), Peking University. The running conditions were set to an acceleration voltage of 10 kV, a beam current of 5 nA, and a working distance of ~10 mm. Compositional X-ray maps were recorded with an integration time of ~360 min.

3.2. Electron microprobe analyses

Mineral compositions were analyzed using a JEOL 8230 electron microprobe analyzer at SESS, Peking University. The SPI 53 mineral standards (U.S.) were adopted for the quantitative analyses (following Li et al., 2018): jadeite for sodium (Na), aluminium (Al), and silicon (Si); rutile for titanium (Ti);

chromium oxide for chromium (Cr); hematite for iron (Fe); rhodonite for manganese (Mn); diopside for magnesium (Mg) and calcium (Ca); sanidine for potassium (K); and nickel silicide for nickel (Ni). The acceleration voltage and beam current were 15 kV and 10 nA, respectively. The beam diameter was 2 μm for all minerals except for calcite (5–10 μm). The PRZ correction was performed at the final calibration stage.

3.3. Raman spectroscopic and microthermometric analyses

Raman spectra were acquired using a Renishaw InVia Reflex microspectrometer at SESS, Peking University. Measurements were conducted on polished thin sections (30 μm thick for mineral analyses and 100 μm thick for fluid inclusion analyses) without any glue or resin. The laser (532 nm) was focused on the sample by a DMLM Leica microscope with a 100-fold objective (numerical aperture (N.A.) = 0.85). Different laser powers were set from an initial 50 mW source for opaque minerals (10%), silicates (50%–100%), carbonates (50%–100%), and fluid inclusions (100%). The spectrometer was calibrated with a synthetic Si wafer.

Fluid inclusion microthermometric studies were carried out using a Linkam THMSG 600 heating–freezing stage mounted onto an Olympus microscope at Key Laboratory of Mineral Resources, Institute of Geology and Geophysics, Chinese Academy of Sciences (IGGCAS). The two-phase (vapor and liquid) fluid inclusions with relatively large sizes were selected to determine the final ice melting temperatures and homogenization temperatures. The heating rates of 0.1–

0.2 °C/min were adopted for the determination when phase transitions were approached. The estimated errors in the measurements are ± 0.1 °C for the melting temperatures and ± 2 °C for the homogenization temperatures. Salinities, pressures at homogenization, and isochore slopes for the fluid inclusions were calculated using the procedures described by Steele-MacInnis et al. (2012).

3.4. *In situ* Sr isotopic analyses

In situ Sr isotopic measurements of dolomite and calcite were performed by Nu Plasma II MC-ICP-MS coupled with a 193-nm ArF excimer laser ablation system (GeoLas HD) at SESS, Peking University (see Lin et al., 2021 for detailed description of the instrument and laser ablation system). Instrumental operating conditions and data acquisition protocols are similar to those described in Ramos et al. (2004) and Yang et al. (2009). The laser ablation was performed using a spot size of ~90 μm, a repetition rate of ~5 Hz, and an energy density of ~10 J/cm^2. The helium (He) gas (with a flow rate of ~0.5 L/min), carrying ablated sample aerosols and passing through the "wire" signal smoothing device (Hu et al., 2012), was merged with argon (Ar) gas before entering the plasma. Prior to each ablation, a 30-s measurement of gas blank was employed to correct for the isobaric interference of krypton (Kr). Correction of rubidium (Rb) was conducted using the natural ratio of $^{85}Rb/^{87}Rb = 2.5926$ with an exponential law, assuming that the mass bias of Rb is identical to that of Sr (e.g., Woodhead et al., 2005). Actually, the studied samples have extremely low $^{87}Rb/^{86}Sr$ values, indicative of the negligible interference of Rb. Previous studies have demonstrated that the

interference of Ca argides and dimers in carbonate minerals is minor and thus has insignificant influence on the accuracy of $^{87}Sr/^{86}Sr$ ratios (e.g., Ramos et al., 2004; Vroon et al., 2008; Yang et al., 2009). Double-charged ions in the samples have extremely low ion signals, suggesting that they play a very limited role in interfering $^{87}Sr/^{86}Sr$ ratios. The instrumental mass bias was corrected using the $^{86}Sr/^{88}Sr$ ratio of 0.1194 with an exponential law. A modern Porites coral (Hainan Island, China) was used as the internal standard to evaluate the accuracy of the analyses, which yielded $^{87}Sr/^{86}Sr$ ratios of 0.709170 ± 0.000016 (2σ, n = 33), in agreement with those obtained by solution-based MC-ICP-MS analyses ($^{87}Sr/^{86}Sr$ = 0.709176 ± 0.000016; Yang et al., 2009). In this study, Sr isotope data with generally comparable ^{88}Sr ion signals higher than ~1 V were selected for dolomite and calcite to minimize the potential influence of composition-induced matrix effects and brucite interference on calcite due to their intergrown textures (Section 4.1). In general, the analyzed $^{87}Sr/^{86}Sr$ ratios of dolomite are close to those obtained by solution-based TIMS analyses for dolomite in surrounding H*P* ophidolomites (Section 4.3; Peng et al., 2020).

3.5. C and O isotopic analyses

Microdrilling was conducted on dolomite and calcite using a standard dentist drill (0.2 mm, 0.5 mm, and 1.0 mm) under the stereomicroscope (SMZ 1500) at State Key Laboratory of Lithospheric Evolution (SKLLE), IGGCAS. Vertical holes were drilled down to thick sections (ca. 0.3–0.5 mm) by increments and at least 2 mg of powder of each selected grain was collected. C and O isotope

compositions of dolomite, calcite, and bulk carbonate were determined using a Thermo Fisher MAT 253 isotope ratio mass spectrometer coupled with a GasBench II peripheral device at SKLLE, IGGCAS, through production of CO_2 after reaction with phosphoric acid. The reaction vial was automatically flushed with high-purity (99.999%) He gas for 10 min at a flow rate of ~0.1 L/min to remove atmospheric contaminants including traces of CO_2 and water (H_2O) vapor. The acid digestion was performed in the GasBench II using continuous flow mode at a temperature of 70 °C, through which the generated CO_2 was transferred by the He carrier gas into the mass spectrometer. In the analyses, $\delta^{18}O$ values of bulk carbonate were not reported because the mixture of dolomite and calcite prevents the accurate back-calculation by using O isotope fractionation factors between the carbonate and phosphoric acid. Standard deviations of $\delta^{13}C$ and $\delta^{18}O$ values were calculated from replicate analyses of an internal laboratory calcite standard, which are better than 0.15‰ and 0.20‰, respectively. The measured $\delta^{13}C$ and $\delta^{18}O$ values are reported relative to the Vienna Pee Dee Belemnite (V-PDB) and Vienna Standard Mean Ocean Water (V-SMOW), respectively.

3.6. Thermodynamic modelling

To evaluate the role of oxygen fugacity (fO_2; log bar unit) and hydrogen fugacity (fH_2; log bar unit) in the reduction process of dolomite (nearly pure; Section 4.1), we calculated the fO_2–fH_2 equilibrium diagram in the Ca–Mg–C–O–H system (with fixed Ca:Mg:C of 1:1:2 in molar ratio) at 8 kbar and 420 °C using Perple_X software (version 6.7.4; Connolly, 2005) and the internally consistent

thermodynamic database of Holland and Powell (1998) revised in 2004 (hp04ver.dat). The *P–T* conditions were chosen based on the onset of retrograde serpentinization in the Tianshan (Li et al., 2007, 2010). Thermodynamic parameters of phases belonging to the system are provided in Supplementary Table S1, most of which are available from literatures (Robie and Hemingway, 1995; Holland and Powell, 1998; Fukui et al., 2003) while the thermal expansion coefficient of portlandite was calculated based on the cell volume changes during heating from Xu et al. (2007). Redox buffers of magnetite–hematite (MH), fayalite–magnetite–quartz (FMQ), and iron–magnetite (IM) were calculated for reference at 8 kbar and 420 °C. The thermodynamic model of H_2O was performed using the Fluids routine (H–O MRK hybrid–EoS) of the Perple_X software, which will be discussed in Section 4.4.

To investigate the equilibrated phase assemblages of reduced ophidolomites during the retrograde serpentinization, we computed *P–T* pseudosections for a representative sample C1534 in the Ca–Fe–Mg–Si–C–O–H system. The applied solid solution models and their sources are provided in Supplementary Table S2. The bulk-rock composition used for the pseudosections was measured by X-ray fluorescence (XRF) spectrometry at the National Research Center for Geoanalysis, Chinese Academy of Geological Science. The contents of major oxides and loss on ignition (LOI) are listed in Table 1, with the analytical uncertainties better than 5%. To specify C as the thermodynamic components, we further derived the effective bulk-rock composition (Table 1) by integrating mineral compositions

and modes, in which the H_2O and CO_2 contents were calculated based on the abundances of hydrous minerals and carbonates in the sample (see Li et al., 2012 and Peng et al., 2020 for similar approaches).

4. RESULTS

4.1. Petrography and mineral chemistry of ophidolomites

The studied ophidolomites consist primarily of antigorite and dolomite, while calcite, brucite, magnetite, and olivine are present as minor or accessory phases. Microstructures show a replacement texture in which dolomite grows at the expense of antigorite (Fig. 2C and D). In most cases, dolomite grains have experienced various degrees of decomposition, resulting in the formation of acicular calcite–brucite intergrowths (Fig. 2E–G). This transformation propagates inside dolomite along microcracks (Fig. 2G), which, together with patches of relict dolomite in calcite products (Fig. 2H), suggests the retrograde decomposition postdating dolomite formation. Olivine occurs as relicts in the antigorite matrix (Fig. 3A) and inclusions (in association with antigorite and brucite) within magnetite (Fig. 3B and C). Magnetite grains, ranging in size from one to several millimeters, commonly enclose a variety of minerals that are dominated by antigorite and dolomite (Fig. 3B). In some of the magnetite-hosted mineral inclusions, the replacement of dolomite by calcite and brucite are observed (Fig. 3D).

Representative mineral compositions of the studied ophidolomites are presented in Table 2. Antigorite and dolomite show nearly identical X_{Mg} (= $Mg/(Mg + Fe)_{molar}$) values of 0.958–0.985 and 0.955–0.991 (Supplementary Fig. S1), respectively, in agreement with the petrographically recognized dolomite growth at the expense of antigorite (Fig. 2C and D). Also, the acicular brucite intergrown with calcite exhibits similar X_{Mg} values of 0.963–0.992 (Supplementary Fig. S1), in accord with the petrographic identification of dolomite transformation into calcite and brucite (Fig. 2E–H). By contrast, olivine displays relatively lower X_{Mg} values of 0.932–0.933, comparable to those of metamorphic olivine (X_{Mg} = 0.91–0.93) in associated UH*P* serpentinites (Supplementary Fig. S1; Shen et al., 2015).

4.2. Petrography, Raman spectroscopy, and microthermometry of fluid inclusions

Abundant fluid inclusions, variable in both shapes (spherical, sub-spherical, and tubular) and sizes (from submicron to ~8 μm), are observed in dolomite in the studied ophidolomites. These fluid inclusions are grouped into fluid inclusion assemblages (FIAs) based on petrographic criteria (Goldstein and Reynolds, 1994; Bodnar, 2003), and two main types of FIAs are further distinguished at room temperatures. Fluid inclusions in the pervasive Type-I FIAs contain vapor and liquid phases and show weak optical contrast to dolomite (Fig. 4A and B). Typically, these two-phase fluid inclusions are liquid-rich and have less variable vapor to liquid ratios of about 5–15 vol% (Fig. 4A and B). Conversely, fluid

inclusions in Type-II FIAs commonly contain a single phase and show strong optical contrast to dolomite (Fig. 4C and D). In most cases, both types of FIAs form trails crosscutting grain boundaries (Fig. 4A–D), indicating their entrapment later than the host dolomite. However, the cloudy appearance and fine grain sizes of calcite–brucite intergrowths (Fig. 2E–H) have significantly hindered the recognition of calcite-hosted fluid inclusions. Despite this, two-phase fluid inclusions are observed in calcite owing to the movement of vapor bubbles inside, which are mostly isolated and randomly distributed, probably reflecting fluid entrapment during the growth of calcite (Fig. 4E–G and Supplementary Fig. S2A and B).

Raman spectroscopic and microthermometric studies were conducted on the fluid inclusions. In Type-I fluid inclusions, the gaseous and liquid species are rich in CH_4 and H_2O, respectively, whereas the strong fluorescence interference of the host carbonates sometimes impedes direct observation of the H_2O peaks (Fig. 5A and B; see also Yang et al., 2018). In contrast, dolomite-hosted Type-II fluid inclusions certainly contain CH_4, while H_2 was occasionally detected (Fig. 5C). In rare cases, calcite and brucite were detected in only a few of dolomite-hosted Type-II fluid inclusions, which, however, cannot be unequivocally considered as daughter minerals (Supplementary Fig. S2C). Overall, Type-I vapor- and liquid-bearing fluid inclusions show relatively consistent final ice melting temperatures (T_m) of –3.6 to –1.3 °C, corresponding to salinities of 2.2–5.9 wt% NaCl (Table 3). Moreover, these two-phase fluid inclusions have generally comparable

homogenization temperatures (T_h) of 180–230 °C, pressures at homogenization (P_h) of 9–27 bar, and isochore slopes (dP/dT) of 14.2–17.0 (Table 3).

4.3. Isotope geochemistry

Representative Sr isotope compositions of dolomite and calcite in the studied ophidolomites are listed in Table 4. Dolomite has $^{87}Sr/^{86}Sr$ ratios of 0.70476–0.70757 (average = 0.70566, n = 50), lower than those of Ordovician–Carboniferous (lifetime of the south Tianshan paleo-ocean; Xia et al., 2014) seawater ($^{87}Sr/^{86}Sr$ = ca. 0.7076–0.7092; Veizer et al., 1999) but similar to those of associated HP ophidolomites and their dolomite separates ($^{87}Sr/^{86}Sr$ = ca. 0.7064–0.7075; Peng et al., 2020) (Fig. 6A). In contrast, calcite shows relatively higher $^{87}Sr/^{86}Sr$ ratios of 0.70867–0.70986 (average = 0.70938, n = 46), which are comparable to those of the seawater as well as serpentinites in the Tianshan (Peng et al., 2020) (Fig. 6A).

Detailed C and O isotope values of dolomite, calcite, and bulk carbonate in the studied ophidolomites are shown in Table 5. Dolomite and calcite have $\delta^{13}C$ values of +9.2‰ ~ +11.7‰ and +7.0‰ ~ +9.0‰, respectively, similar to those of bulk carbonate ($\delta^{13}C$ = +8.6‰ ~ +10.3‰) (Fig. 6B). These C isotope values are significantly higher than $\delta^{13}C$ of marine carbonates (–3‰ ~ +3‰; Hoefs, 2009) and carbonate-bearing but CH_4-absent lithologies from the Tianshan (mostly ≤ 0‰; van der Straaten et al., 2012; Collins et al., 2015; Peng et al., 2018, 2020; Zhu et al., 2018) (Fig. 6B). Moreover, dolomite and calcite display $\delta^{18}O$ values of +8.1‰ ~ +9.6‰ and +8.4‰ ~ +12.6‰, respectively (Fig. 6B).

4.4. Thermodynamic results

In the fO_2–fH_2 equilibrium diagram of Fig. 7A, the stability field of dolomite, shrinking with the elevated log fH_2 values, extends down to log fO_2 = –29.1 (ΔFMQ –2.5, where ΔFMQ refers to the deviation of log fO_2 from the FMQ buffer) at log fH_2 < 1.4. The boundary between dolomite and the phase assemblage of calcite + brucite + CH_4 is constrained at log fO_2 = –27.3 ~ –20.6 (ΔFMQ –0.7 ~ +6.0) and log fH_2 = 0.3 ~ 1.4. In the H–O system, pure H_2O (y_{H2O} = 1, where y_{H2O} is the molar fraction of H_2O in fluids) is characterized by an ideal X_O (= O/(O + H)$_{molar}$) of 1/3. In the vicinity of this value, only negligible amounts of O_2 or H_2 is encompassed due to the fO_2- and fH_2-dependent H_2O dissociation, representing slightly oxidized or reduced conditions, respectively (e.g., Connolly, 1995). In this study, we superposed the thermodynamically calculated model of slightly reduced H_2O at X_O = 0.33 ~ 1/3 on the fO_2–fH_2 diagram (Fig. 7A), based on the inferred serpentinization-derived fluids responsible for dolomite reduction (Section 5.2) and the widely distributed aqueous fluid inclusions but the sporadically detected H_2 in the studied rocks (Figs. 4 and 5; Section 4.2). Although the reactive reduced fluids may potentially contain small amounts of other components (see below), they do not significantly affect our model calculations performed in the H–O system. Firstly, the fluids are likely CO_2-poor, because fluid inclusions do not contain detectable CO_2 in the studied ophidolomites and carbonate minerals are not widely distributed in surrounding rodingites formed by interactions with fluids related to the retrograde serpentinization (Li et al., 2007,

2010; Shen et al., 2012, 2016). Alternatively, preexisting C-bearing species (e.g., CO_2) in the fluids may have been reduced into CH_4 during the serpentinization, as recorded in partially serpentinized rocks in comparable metamorphic settings (Sachan et al. 2007; Vitale Brovarone et al., 2020; Boutier et al., 2021). In this scenario, we set C concentrations of 0.001–0.05 molal in the fluids equilibrated with carbonate-undersaturated to carbonate-saturated serpentinites at the studied *P*–*T* conditions (Vitale Brovarone et al., 2020), and the calculated mole fractions of H_2O are significantly higher than those of other molecular species (e.g., CH_4, CO_2, and H_2) at X_O close to 1/3 (Supplementary Fig. S3). Secondly, even though halogens (e.g., chlorine, Cl) commonly occur in serpentinizing fluids that may decrease the activity of H_2O (e.g., Lamadrid et al., 2017, 2021), CH_4-bearing aqueous fluid inclusions in the studied rocks contain relatively low salinities of 2.2–5.9 wt% NaCl (Table 3). These salinities correspond to H_2O mole fractions of ca. 0.981–0.993 in the fluids, and thus have a negligible effect on the activity of H_2O (e.g., Aranovich and Newton, 1996). Thirdly, thermodynamic calculations predicted very low electrolyte concentrations of ca. 0.004–0.03 molal (mainly Si, Mg, and Ca) in the fluids equilibrated with the Tianshan serpentinites during retrogression (Supplementary Fig. S4), indicating that these electrolytic solutes cannot profoundly affect the homogeneous equilibria among the dominant molecular species and thus the application of molecular fluid models (Connolly and Galvez, 2018). It is therefore likely that the possible existence of dissolved species (e.g., CO_2, Cl, and other electrolytes) in the reactive reduced fluids have

only minor effects on the calculations in our model. The fO_2–fH_2 equilibrium diagram illustrates that an infiltration of H_2O-rich fluids characterized by relatively high fH_2 values can contribute to abiotic CH_4 formation through dolomite reduction at the studied P–T conditions (Fig. 7A). For instance, at X_O = 0.3333323 (corresponding to y_{H2O} = 0.999995 and y_{H2} = 0.000005; star in Fig. 7A), the H_2O-rich fluids buffered at log fO_2 = –26.0 (ΔFMQ +0.6) show a log fH_2 value of 0.8 and equilibrate with the phase assemblage of calcite + brucite + CH_4.

The calculated P–T pseudosection for the reduced ophidolomite (Sample C1534) at log fO_2 = –26.0 and log fH_2 = 0.8 (star in Fig. 7A) suggests that the observed phase assemblage of antigorite + brucite + calcite + magnetite + CH_4 can be predicted at 7–9 kbar and 410–430 °C (Fig. 7B). Similar results computed at log fO_2 = –25.8 and log fH_2 = 0.7 (Supplementary Fig. S5A) indicate that variable fO_2 and fH_2 of the fluids in equilibrium with calcite + brucite + CH_4 have no significant effects on the P–T pseudosection. However, since the constrained log fO_2 and log fH_2 values for these calculations depend on and vary with P–T conditions, uncertainties may occur in the phase stabilities predicted at P–T conditions considerably higher or lower than 7–9 kbar and 410–430 °C in Fig. 7B and Supplementary Fig. S5A. Further, the P–T pseudosection was calculated for the sample without fO_2 and fH_2 constraints, demonstrating that the unreduced mineral assemblage of antigorite + brucite + dolomite + calcite + magnetite can remain stable at the studied P–T conditions (Supplementary Fig. S5B).

5. DISCUSSION

Ophicarbonates play a potential role in contributing to the subduction influx of C (Dasgupta and Hirschmann, 2010; Alt et al., 2012, 2013) and recording the mechanisms of C mobility and percolation at convergent plate boundaries (Scambelluri et al., 2016; Vitale Brovarone et al., 2017; Piccoli et al., 2018; Cannaò et al., 2020; Peng et al., 2020). Marine-originated ophicarbonates (mainly ophicalcites) are typically characterized by Ca-carbonate matrix cementing serpentinite clasts or Ca-carbonate veins filling fractured serpentinites (Bonatti et al., 1974; Früh-Green et al., 2003; Schwarzenbach et al., 2013; Clerc et al., 2014; Lafay et al., 2017). Subseafloor mixing zones between these pristine ophicalcites and serpentinites may have served as incubators for biological communities in the hydrated oceanic mantle, offering insights into deep chemolithoautotrophic life (Klein et al., 2015). Moreover, H*P* carbonation of subduction-zone serpentinites through interactions with slab-released CO_2-bearing fluids has been increasingly recognized, providing implications for the distribution of subducted C (Scambelluri et al., 2016; Piccoli et al., 2018; Peng et al., 2020). The Changawuzi H*P* ophidolomites (15–25 kbar and 550–600 °C) have been studied in detail by Peng et al. (2020), which are characterized by carbonate growth at the expense of silicates in the host serpentinites and record interactions with CO_2-bearing fluids emanating from metamafic and/or metasedimentary rocks in the subduction zone. Similarly, the replacement of metamorphic antigorite by dolomite (Fig. 2C and D) and their compositional inheritance (e.g., X_{Mg} values; Supplementary Fig. S1)

in the studied CH_4-bearing ophidolomites point to dolomite formation through interactions between CO_2-bearing fluids and serpentinites during metamorphism. This is reflected by Sr isotope compositions of dolomite in these rocks considerably distinct from those of seawater in the south Tianshan paleo-ocean but generally similar to those of associated H*P* ophidolomites and their dolomite separates (Fig. 6A), likely inheriting the low $^{87}Sr/^{86}Sr$ values of subducted carbonate-bearing lithologies in the Tianshan (Peng et al., 2020). Microstructures, mineral compositions, and Sr isotopic signatures of the studied CH_4-bearing ophidolomites are comparable to those of H*P* ophidolomites in the same study area (Peng et al., 2020), indicating that they likely record the consistent H*P* carbonation of serpentinites in the subduction zone. Even though obtaining precise *P*–*T* constraints for dolomite formation in the studied rocks is relatively difficult, it may not considerably affect the following discussion with respect to dolomite reduction and abiotic CH_4 generation in the subduction zone.

5.1. Abiotic CH_4 generation through dolomite reduction

Intergrowths of calcite and brucite in natural rocks (Fig. 2E–H) are relatively hard to be preserved because these fine and soluble minerals are easily removed by an abundance of circulating fluids (Berg, 1986). The retrograde decomposition of dolomite into calcite–brucite intergrowths was observed in mantle wedge ultramafic rocks and interpreted as Reaction (1), which occurred by infiltration of H_2O at oxidized conditions (Förster et al., 2017; Consuma et al., 2020):

$$\underset{\text{dolomite}}{CaMg(CO_3)_2} + H_2O = \underset{\text{calcite}}{CaCO_3} + \underset{\text{brucite}}{Mg(OH)_2} + CO_2. \quad (1)$$

In this study, by contrast, the pervasive occurrence of $CH_4 \pm H_2O \pm H_2$ in dolomite- and calcite-hosted fluid inclusions (Figs. 4 and 5) likely suggests reduced aqueous fluids responsible for the decomposition of dolomite. Nevertheless, the limited distribution of H_2 in the fluid inclusions (Section 4.2) is probably indicative of its minor proportion in the reactive aqueous fluids, or, alternatively, ascribed to several other potential processes (see below). Thermodynamic calculations further demonstrate that an infiltration of H_2O-rich fluids, characterized by a relatively high $\log fH_2$ value of 0.8 but containing a low H_2 molar fraction of 0.000005 (star in Fig. 7A), can result in the transformation of dolomite into the phase assemblage of calcite + brucite + CH_4, which is expressed by the fH_2-dependent Reaction (2):

$$\underset{\text{dolomite}}{CaMg(CO_3)_2} + 4H_2 = \underset{\text{calcite}}{CaCO_3} + \underset{\text{brucite}}{Mg(OH)_2} + CH_4 + H_2O. \quad (2)$$

This CH_4-generating reaction is endorsed by the notably high $\delta^{13}C$ values of carbonates in the studied rocks (Fig. 6B). The positive shift in $\delta^{13}C$ is exactly opposite to the typical C isotopic trend related to decarbonation reactions and/or carbonate–organic matter re-equilibrations as also recorded in the Tianshan (Fig. 6B; Collins et al., 2015; Zhu et al., 2018). Similar high $\delta^{13}C$ values were interpreted as evidence for carbonate reduction forming graphite (Galvez et al., 2013b) or abiotic CH_4 (Vitale Brovarone et al., 2017) in comparable metamorphic settings. Based on $\delta^{13}C$ of calcite (Table 5) and the equilibrium fractionation

factor between calcite and CH_4 ($ln\alpha(CaCO_3–CH_4)$ = +15.0‰ ~ +16.0‰ at 410–430 °C; Bottinga, 1969), we calculated C isotope compositions of CH_4 ranging from –9.0‰ to –6.0‰. These values fit the range of C isotope compositions of abiotic CH_4 from worldwide occurrences, which display $\delta^{13}C$ values typically higher than ca. –25‰ (e.g., Ueno et al., 2006; Etiope et al., 2011). Considering that dolomite in the studied ophidolomites is likely related to the H*P* carbonation of serpentinites (see above), its heavy $\delta^{13}C$ values relative to those in associated H*P* ophidolomites (Fig. 6B) are probably attributed to an additional reduction process of dolomite other than Reaction (2). In this process, dolomite may have been decomposed into CH_4 together with aqueous species such as Ca^{2+} and Mg^{2+}, which represents the reduction of dissolved C-bearing species (e.g., CO_3^{2-}, HCO_3^-, and/or $CO_{2,aq}$) of dolomite (see Frezzotti et al., 2011; Ague and Nicolescu, 2014; and Facq et al., 2014 for carbonate dissolution in subduction zones). In addition to the potential dissolution-induced dolomite reduction, other processes resulting in C isotopic enrichment of the residual dolomite may also be possible.

It is apparent that Reaction (2) essentially reflects a H_2O-triggered decarbonation process of dolomite (Reaction (1)) coupled with a coinstantaneous fH_2-dependent reduction process of CO_2 (Reaction (3)):

$$CO_2 + 4H_2 = CH_4 + 2H_2O. \quad (3)$$

In this study, however, the decarbonation of dolomite is not spontaneous in reduced environments and thus seems unlikely to proceed independently prior to the reduction of CO_2 (see below). Firstly, the fluid inclusions do not contain

detectable CO_2 as the intermediate product, in which CH_4 occurs as the dominant C-bearing species instead. The isolated and randomly distributed CH_4-bearing fluid inclusions in calcite may provide further evidence for the simultaneous production of CH_4 and calcite through dolomite decomposition (Fig. 4E–G and Supplementary Fig. S2A and B). Secondly, the retrograde serpentinization responsible for abiotic CH_4 formation (Section 5.2) started at 7–9 kbar and 410–430 °C and propagated to lower *P*–*T* conditions (e.g., 2–10 kbar and 250–350 °C; Li et al., 2007, 2010), indicating that dolomite decarbonation, if it exists, should take place at oxidized conditions prior to the retrograde serpentinization. In this scenario (i.e., $P > 7$–9 kbar and $T > 410$–430 °C), aragonite is likely to replace calcite as the dominant Ca-carbonate products (cf. the calcite–aragonite transition in Fig. 8; Johannes and Puhan, 1971), inconsistent with the observed calcite–brucite intergrowths in the studied ophidolomites (Fig. 2E–H). Thirdly, the elevated C isotope values of calcite, contrary to the negative shift of $\delta^{13}C$ derived from carbonate decarbonation (Fig. 6B), provide geochemical constraints on the equilibrium between calcite and CH_4 in the studied ophidolomites (see above). An alternative explanation may exist for these results that dolomite has recorded ^{13}C enrichment (e.g., through dissolution-induced reduction; see above) prior to the decoupled dolomite decarbonation and CO_2 reduction processes, but such cyclic redox transformations (i.e., reduction–oxidation–reduction) are not reported in the study area (Li et al., 2007, 2010).

Although our model calculations demonstrate that H_2O-rich fluids at relatively high fH_2 (e.g., y_{H2O} = 0.999995 at log fH_2 = 0.8; star in Fig. 7A) can create favorable conditions for dolomite reduction and abiotic CH_4 generation, the possibility of carbonate methanation by H_2-rich fluids cannot be excluded. The latter case has been reported in subducted ophicalcites in the Western Alps, recording a H_2-induced calcite methanation process in which the equilibrated fluids are characterized by dominant CH_4 while $y_{H2O} = y_{H2}$ at $X_O < 0.03$ at 7 kbar and 350 °C (Vitale Brovarone et al., 2017). In this scenario, H_2 is not pervasively detected by Raman spectroscopy in fluid inclusions in the studied rocks (Figs. 4 and 5; Section 4.2) probably because it has been largely consumed by carbonate reduction to CH_4 (e.g., Grozeva et al., 2020). Alternatively, H_2 could potentially occur in the fluid inclusions but the Raman peaks have been severely obscured by the strong fluorescence of the host carbonates (Fig. 5). Overall, there is no petrographic evidence for post-entrapment re-equilibrations of the fluid inclusions (e.g., stretching, leakage, and decrepitation), as supported by their relatively consistent vapor to liquid ratios (Fig. 4A and B; Section 4.2), homogenization temperatures (Table 3), and Raman peak positions of gaseous CH_4 (Supplementary Table S3) within an individual FIA (e.g., Bodnar, 2003; Lin et al., 2007). Concentrations of molecular species as a function of X_O in the graphite-buffered COH system calculated at 7 kbar and 350 °C (Vitale Brovarone et al., 2017; see Supplementary Fig. S6 for similar calculations at the studied *P*–*T* conditions) illustrate that mole fractions of H_2O in the fluids, relative to CH_4 and

H_2, progressively increase with X_O (until at X_O = 1/3). Such calculations suggest that determination of proportions of these species in the equilibrated fluids may provide important insights into the reduced nature of the reactive fluids (i.e., H_2O-rich fluids at relatively high fH_2 *vs.* H_2-rich fluids).

5.2. Reduced fluid source(s) and fluid inclusion entrapment

The reactive reduced fluids are likely associated with retrograde serpentinization in the Tianshan, during which the observed phase assemblage in the studied rocks can remain stable (Fig. 7B and Supplementary Fig. S5). Even though fluid source(s) responsible for the retrograde serpentinization is(are) largely unresolved (Li et al., 2007, 2010), the preservation of Sr and O isotopic signatures of seawater in the Tianshan serpentinites (Scicchitano et al., 2018; Peng et al., 2020) suggests that these rocks may record interactions with fluids migrating upward from serpentinite dehydration at greater depths (see also Angiboust et al., 2014 and Piccoli et al., 2018). Serpentinization of olivine provides a potential source for H_2, together with the concomitant formation of magnetite (Reaction (4); e.g., McCollom and Bach, 2009; Klein et al., 2013, 2020).

$$(Mg,Fe)_2SiO_4 + H_2O \rightarrow (Mg,Fe)_3Si_2O_5(OH)_4 + (Mg,Fe)(OH)_2 + Fe_3O_4 + H_2. \quad (4)$$

olivine — serpentine — brucite — magnetite

Although the possibility for serpentinization of olivine to produce H_2 at high temperatures (400–600 °C) has been questioned (Evans, 2010), recent studies show that magnetite formation and H_2 generation through H*P* serpentinization may be common under several subduction zone conditions (Vitale Brovarone et

al., 2020; Boutier et al., 2021). Thus, olivine relicts in the antigorite matrix (Fig. 3A), as well as the occurrence of olivine (in association with antigorite and brucite) and dolomite decomposition within magnetite (Fig. 3B–D), suggest that the studied ophidolomites may have acted as a possible H_2 source for the reduction process. Alternatively, the reduced fluids may be externally derived from the rehydration of surrounding serpentinites, which contain ~25 vol% metamorphic olivine (Shen et al., 2015). Moreover, the elevated $^{87}Sr/^{86}Sr$ ratios of calcite, decoupled from dolomite but in general agreement with the Tianshan serpentinites that have largely inherited Sr isotope values of the seawater (Fig. 6A; Peng et al., 2020), likely reflect Sr isotope exchange with the serpentinizing fluids during dolomite reduction.

In the studied rocks, a majority of dolomite-hosted fluid inclusions form trails crosscutting grain boundaries (Fig. 4A–D), indicating that they were trapped along fractures of dolomite and preserved through subsequent healing of these fractures. The relative timing of fluid entrapment can be obtained by fluid inclusion isochores intersecting the retrograde path of the Chinese southwestern Tianshan (Tan et al., 2017), which constrained *P*–*T* conditions of about 1–3 kbar and 250–350 °C (Fig. 8). The *P*–*T* constraints, lower than 7–9 kbar and 410–430 °C, suggest that entrapment of the fluid inclusions postdates the onset of dolomite reduction (Fig. 8). Based on the localized alteration of dolomite (Fig. 2), we infer that the reactive reduced fluids may be limited and have been largely consumed by dolomite after the reduction started, leading to the stability of relict reactants

until the fractures were generated to provide fluid pathways and subsequently healed to preserve the fluid inclusions. This is in agreement with our petrographic observations that dolomite-hosted fluid inclusions are nearly devoid of calcite and brucite daughter minerals representative of dolomite reduction within the inclusions (Section 4.2). Given that the retrograde serpentinization responsible for dolomite reduction could propagate to relatively lower *P*–*T* conditions (e.g., 2–10 kbar and 250–350 °C; Li et al., 2007, 2010), the possibility may exist that the timing of fluid inclusion trapping is slightly later than or close to that of abiotic CH_4 formation. Under this circumstance, the reduction process of dolomite probably came to a halt due to the exhaustion of the reactive reduced fluids (see above), closely followed by fluid entrapment along the fractures. Note that this possibility depends primarily on *P*–*T* conditions for the propagation of the retrograde serpentinization, which, however, remain uncertain despite the calculations by Li et al. (2007, 2010) based on a few reactions observed in serpentinites and associated rodingites. Uncertainties may mainly derive from the controversial *P*–*T* conditions for the transformation of chrysotile into antigorite (Evans et al., 1976; Scambelluri et al., 2004; Li et al., 2007, 2010) and the ignorance of several potential reactions (e.g., the lizardite to antigorite transition; Guillot et al., 2015) in rocks for the constraints (Fig. 8).

5.3. Implications for C mobility in subduction zones

Laboratory studies demonstrated that carbonate aqueous reduction at fO_2 far below the FMQ buffer (e.g., the IM or iron–wüstite (IW) buffer) under H*P*

conditions is a potential pathway for significant production of abiotic CH_4 in subduction zones (Lazar et al., 2014; Mukhina et al., 2017). Moreover, field-based investigations constrained a relatively wide range of log fO_2 values for H*P* abiotic formation of CH_4 via carbonate reduction in ophicalcites from the Western Alps (ΔFMQ –6.0 ~ –3.0 at 1 GPa and 400 °C; Vitale Brovarone et al., 2017) and in carbonated eclogites from the Tianshan (ΔFMQ –2.5 at 2.5 GPa and 550 °C; Tao et al., 2018a). In the present study, thermodynamic simulations suggest that abiotic CH_4 generation through dolomite aqueous reduction can occur at fO_2 slightly lower than or even close to the FMQ buffer (Fig. 7A). The stability of CH_4-bearing fluids at FMQ conditions is reflected by a three-dimensional *P*–*T*–log fO_2 diagram calculated for graphite/diamond-saturated COH fluids (Tumiati and Malaspina, 2019), displaying that the FMQ surface is below the maximum H_2O activity surface where CH_4 is the dominant C-bearing species under the studied *P*–*T* conditions. Furthermore, experiments conducted on H*P* aqueous reduction of organic matter demonstrated that CH_4-bearing fluids in equilibrium with graphite can stabilize at fO_2 approaching the FMQ buffer (i.e., the Co–CoO or Ni–NiO buffer at 2.5 GPa and 600–700 °C; Li, 2017). In the studied samples, however, graphite was sporadically detected in the cloudy calcite–brucite intergrowths (Supplementary Fig. S7), which may be attributed to the high fH_2 conditions (see below).

Graphite has been observed in several CH_4-absent (Malvoisin et al., 2012; Galvez et al., 2013a, b; Zhu et al., 2020) or CH_4-bearing (Vitale Brovarone et al.,

2017, 2020; Tao et al., 2018a) lithologies in subduction zones, formed by carbonate anhydrous graphitization or precipitating from the reduced COH fluids. Compared with carbonate minerals (e.g., Kelemen and Manning, 2015), graphite represents a relatively stable phase that may transfer subducted C into the deep Earth (Galvez et al., 2013a; Duncan and Dasgupta, 2017; Eguchi et al., 2020), while recent studies suggest that graphite could be partly dissolved in subduction-zone fluids (Tumiati et al., 2017, 2020 and references therein). In our study, however, the widespread occurrence of CH_4 compared to graphite illustrates that the equilibrium between graphite and CH_4 may be largely controlled by fH_2 (Fig. 7A), implying that an increase in fH_2 would contribute to the transformation of graphite into CH_4 at convergent plate boundaries. This is in accord with the microstructure-based recognition of an additional abiotic CH_4-forming event in reduced ophicalcites from the Western Alps, attributed to H_2-induced reduction of the newly formed graphite during ascent of the slab (Vitale Brovarone et al., 2017). Moreover, experiments performed on the hydrogenation of graphite at high *P*–*T* conditions (5.0–5.5 GPa and >1500 °C) yielded considerable CH_4, indicating that fH_2 may play an important role in governing abiotic CH_4 genesis in deep subduction zones (Sharma et al., 2009). Indeed, graphite has a very low content or nearly absent in several CH_4–H_2-bearing serpentinites in subduction zones (Peretti et al., 1992; Vitale Brovarone et al., 2020), in agreement with the CH_4–H_2–H_2O equilibrated region below the graphite saturation curve predicted by the isobaric–isothermal C–O–H diagram (e.g., Holloway, 1984).

While the reduction in our study happened during exhumation of the slab, the proposed *P–T* estimates are similar to those of carbonate reduction during shallow subduction in comparable metamorphic settings (Malvoisin et al., 2012; Galvez et al., 2013a, b; Vitale Brovarone et al., 2017; Giuntoli et al., 2020), which are in general accord with the prograde *P–T* paths of subduction zones predicted by thermal models (Syracuse et al., 2010) and metamorphic rocks (Penniston-Dorland et al., 2015) (Fig. 9A). Thus, the reduction process of dolomite described here may have implications for subducted C mobility. Laboratory experiments and field observations provide evidence for dolomite formation through mineral carbonation in subseafloor serpentinization systems (Grozeva et al., 2017), suggesting that subduction of these hydrothermally altered oceanic rocks represents a potential dolomite source in downgoing slabs. Indeed, dolomite, despite its variable contents (ca. 5–50 vol%), is not uncommon in several slab- and mantle wedge-forming lithologies including metaultramafic, metamafic, and metasedimentary rocks (e.g., Li et al., 2012, 2014; Tao et al., 2014, 2018b; Falk and Kelemen, 2015; Zhu et al., 2018). Furthermore, mounting field evidence, as well as thermodynamic modelling, suggests that serpentinization of ultramafic rocks can happen at relatively shallow depths (ca. 20–30 km) in subducted slabs, or even up to ca. 70–80 km (Li et al., 2007, 2010; Vitale Brovarone et al., 2017, 2020; Lazar, 2020). Therefore, an infiltration of these serpentinization-derived reduced fluids would be conducive to dolomite reduction and abiotic CH_4 generation during shallow subduction, which may represent a feasible mechanism

for the mobility of subducted C (Fig. 9B). Moreover, release of such deep-sourced reduced fluids might support the hypothesis that subduction zones potentially provide energy to sustain subsurface chemosynthetic microbial life at habitable temperatures in the overlying forearc (e.g., Curtis et al., 2013; Plümper et al., 2017; Fryer et al., 2020; Lazar, 2020; Vitale Brovarone et al., 2020; Wheat et al., 2020). However, uncertainties remain regarding the implications presented here, particularly under circumstances where the scale and extent of dolomite reduction are insufficiently quantified.

6. CONCLUSIONS

Reduction of ophidolomites in the Chinese southwestern Tianshan H*P*–UH*P* metamorphic belt provides new insights into abiotic CH_4 generation in subduction zones. Petrological characteristics, Raman spectroscopic and microthermometric data of fluid inclusions, Sr and C isotope compositions, and thermodynamic results demonstrate dolomite reduction into the phase assemblage of calcite + brucite + CH_4, likely related to retrograde serpentinization starting at 7−9 kbar and 410−430 °C in the subduction zone. The onset of dolomite reduction is prior to fluid entrapment that happened at about 1–3 kbar and 250–350 °C, leading to the widespread distribution of secondary fluid inclusions along healed fractures of dolomite. Model calculations suggest that an infiltration of H_2O-rich fluids at relatively high fH_2 (e.g., $y_{H2O} = 0.999995$ at $\log fH_2 = 0.8$) can contribute to this reduction process, but the possibility of carbonate methanation by H_2-rich fluids

cannot be excluded. The abundant CH_4-bearing fluid inclusions in these rocks indicate that fH_2 probably plays an important role in regulating the speciation of subducted C, implying that an increase in fH_2 may accelerate abiotic formation of CH_4 through dolomite reduction at convergent plate boundaries. Thus, alteration of dolomite-bearing lithologies represents a potential mechanism for abiotic synthesis of CH_4 in subduction zones, which may have implications for the mobility of subducted C.

ACKNOWLEDGEMENTS

This work was funded by the National Key Research and Development Program of China (No. 2019YFA0708501), the National Natural Science Foundation of China (No. 41520104004), and the Scientific Research Foundation of Pilot National Laboratory for Marine Science and Technology (Qingdao) (No. JCZX202011). Simone Tumiati acknowledges support from the Italian program MIUR PRIN (No. 2017ZE49E7_002). Alberto Vitale Brovarone was supported by the ERC CoG "DeepSeep" (No. 864045), an ANR T-ERC grant (No. LS 171301), and a MIUR Levi Montalcini grant; by the Deep Carbon Observatory (DCO) Deep Energy community; and by the Richard Lounsbery foundation. Discussions with James Connolly, Thomas Bader, Wen Zhang, Yueheng Yang, Enrico Cannaò, Ryosuke Oyanagi, Xiaoxia Li, Xia Zhang, and Shujie Wang are highly appreciated. We thank Yang Wang and Zhicheng Liu for their help during fieldwork, and Hongrui Ding, Liangliang Huang, Hongwei Li, Xiangtian Jin, Nan

Li, Xiaoli Li, and Jiangqing Liu for their patient assistance during sample analyses. The authors are grateful to anonymous reviewers (three for a very early draft and three for a more recent draft) for their detailed and constructive comments and to Frieder Klein (Associate Editor) for his careful editorial handling and helpful suggestions.

APPENDIX A. SUPPLEMENTARY MATERIAL

Supplementary data to this article can be found online at https://doi.org/XXXX.

RESEARCH DATA

All research data used in this study are included in tables and the appendix file.

REFERENCES

Ague J. J. and Nicolescu S. (2014) Carbon dioxide released from subduction zones by fluid-mediated reactions. *Nat. Geosci.* **7**, 355–360.

Alt J. C., Garrido C. J., Shanks W. C., Turchyn A., Padrón-Navarta J. A., López Sánchez-Vizcaíno V., Gómez-Pugnaire M. T. and Marchesi C. (2012) Recycling of water, carbon, and sulfur during subduction of serpentinites: a stable isotope study of Cerro del Almirez, Spain. *Earth Planet. Sci. Lett.* **327–328**, 50–60.

Alt J. C., Schwarzenbach E. M., Früh-Green G. L., Shanks W. C., Bernasconi S. M., Garrido C. J., Crispini L., Gaggero L., Padrón-Navarta J. A. and Marchesi C. (2013) The role of serpentinites in cycling of carbon and sulfur: seafloor serpentinization and subduction metamorphism. *Lithos* **178**, 40–54.

Angiboust S., Pettke T., De Hoog J. C. M., Caron B. and Oncken O. (2014) Channelized fluid flow and eclogite-facies metasomatism along the subduction shear zone. *J. Petrol.* **55**, 883–916.

Arai S., Ishimaru S. and Mizukami T. (2012) Methane and propane micro-inclusions in olivine in titanoclinohumite-bearing dunites from the Sanbagawa high-P metamorphic belt, Japan: Hydrocarbon activity in a subduction zone and Ti mobility. *Earth Planet. Sci. Lett.* **353**, 1–11.

Aranovich L. Y. and Newton R. C. (1996) H_2O activity in concentrated NaCl solutions at high pressures and temperatures measured by the brucite–periclase equilibrium. *Contrib. Mineral. Petrol.* **125**, 200–212.

Berg G. W. (1986) Evidence for carbonate in the mantle. *Nature* **324**, 50–51.

Bodnar R. J. (2003) Reequilibration of fluid inclusions. In *Fluid Inclusions: Analysis and Interpretation* (eds. I. Samson, A. Anderson and D. Marshall). Mineral Association of Canada, Short Course 32. pp. 213–230.

Bonatti E., Emiliani C., Ferrera G., Honnorez J. and Rydell H. (1974) Ultramafic-carbonate breccias from the equatorial Mid Atlantic Ridge. *Mar. Geol.* **16**, 83–102.

Bottinga Y. (1969) Calculated fractionation factors for carbon and hydrogen isotope exchange in the system calcite–carbon dioxide–graphite–methane–hydrogen–water vapor. *Geochim. Cosmochim. Acta* **33**, 49–64.

Boutier A., Vitale Brovarone A., Martinez I., Sissmann O. and Mana S. (2021) High-pressure serpentinization and abiotic methane formation in metaperidotite from the Appalachian subduction, northern Vermont. *Lithos* **396–397**, 106190.

Cannaò E., Scambelluri M., Bebout G. E., Agostini S., Pettke T., Godard M. and Crispini L. (2020) Ophicarbonate evolution from seafloor to subduction and implications for deep-Earth C cycling. *Chem. Geol.* **546**, 119626.

Charlou J. L., Donval J. P., Fouquet Y., Jean-Baptiste P. and Holm N. (2002) Geochemistry of high H_2 and CH_4 vent fluids issuing from ultramafic rocks at the Rainbow hydrothermal field (36°14'N, MAR). *Chem. Geol.* **191**, 345–359.

Charlou J. L., Donval J. P., Konn C., Ondréas H., Fouquet Y., Jean-Baptiste P. and Fourré E. (2010) High production and fluxes of H_2 and CH_4 and evidence of abiotic hydrocarbon synthesis by serpentinization in ultramafic-hosted hydrothermal systems on the Mid-Atlantic Ridge. In *Diversity of Hydrothermal Systems on Slow Spreading Ocean Ridges* (eds. P. A. Rona, C. W. Devey, J. Dyment and B. J. Murton). American Geophysical Union, Washington, DC. pp. 265–296.

Clerc C., Boulvais P., Lagabrielle Y. and de Saint Blanquat M. (2014) Ophicalcites from the northern Pyrenean belt: a field, petrographic and stable isotope study. *Int. J. Earth Sci.* **103**, 141–163.

Collins N. C., Bebout G. E., Angiboust S., Agard P., Scambelluri M., Crispini L. and John T. (2015) Subduction zone metamorphic pathway for deep carbon cycling: II. Evidence from HP/UHP metabasaltic rocks and ophicarbonates. *Chem. Geol.* **412**, 132–150.

Connolly J. A. D. (1995) Phase diagram methods for graphitic rocks and application to the system C–O–H–FeO–TiO_2–SiO_2. *Contrib. Mineral. Petrol.* **119**, 94–116.

Connolly J. A. D. (2005) Computation of phase equilibria by linear programming: A tool for geodynamic modeling and its application to subduction zone decarbonation. *Earth Planet. Sci. Lett.* **236**, 524–541.

Connolly J. A. D. and Galvez M. E. (2018) Electrolytic fluid speciation by Gibbs energy minimization and implications for subduction zone mass transfer. *Earth Planet. Sci. Lett.* **501**, 90–102.

Consuma G., Braga R., Giovanardi T., Bersani D., Konzett J., Lugli F., Mazzucchelli M. and Tropper P. (2020) *In situ* Sr isotope analysis of mantle

carbonates: Constraints on the evolution and sources of metasomatic carbon-bearing fluids in a paleo-collisional setting. *Lithos* **354–355**, 105334.

Curtis A. C., Wheat C. G., Fryer P. and Moyer C. L. (2013) Mariana forearc serpentinite mud volcanoes harbor novel communities of extremophilic *Archaea*. *Geomicrobiol. J.* **30**, 430–441.

Dasgupta R. and Hirschmann M. M. (2010) The deep carbon cycle and melting in Earth's interior. *Earth Planet. Sci. Lett.* **298**, 1–13.

Duncan M. S. and Dasgupta R. (2017) Rise of Earth's atmospheric oxygen controlled by efficient subduction of organic carbon. *Nat. Geosci.* **10**, 387–392.

Eguchi J., Seales J. and Dasgupta R. (2020) Great Oxidation and Lomagundi events linked by deep cycling and enhanced degassing of carbon. *Nat. Geosci.* **13**, 71–76.

Etiope G. and Schoell M. (2014) Abiotic gas: Atypical, but not rare. *Elements* **10**, 291–296.

Etiope G. and Sherwood Lollar B. (2013) Abiotic Methane on Earth. *Rev. Geophys.* **51**, 276–299.

Etiope G., Schoell M. and Hosgörmez H. (2011) Abiotic methane flux from the Chimaera seep and Tekirova ophiolites (Turkey): Understanding gas exhalation from low temperature serpentinization and implications for Mars. *Earth Planet. Sci. Lett.* **310**, 96–104.

Evans B. W. (2010) Lizardite versus antigorite serpentinite: Magnetite, hydrogen, and life(?). *Geology* **38**, 879–882.

Evans K. A. (2012) The redox budget of subduction zones. *Earth Sci. Rev.* **113**, 11–32.

Evans B. W., Johannes W., Oterdoom H. and Trommsdorff V. (1976) Stability of chrysotile and antigorite in the serpentine multisystem. *Schweiz. Mineral. Petrogr. Mitt.* **56**, 79–93.

Facq S., Daniel I., Montagnac G., Cardon H. and Sverjensky D. A. (2014) *In situ* Raman study and thermodynamic model of aqueous carbonate speciation in equilibrium with aragonite under subduction zone conditions. *Geochim. Cosmochim. Acta* **132**, 375–390.

Falk E. S. and Kelemen P. B. (2015) Geochemistry and petrology of listvenite in the Samail ophiolite, Sultanate of Oman: Complete carbonation of peridotite during ophiolite emplacement. *Geochim. Cosmochim. Acta* **160**, 70–90.

Förster B., Braga R., Aulbach S., Lo Pò D., Bargossi G. M. and Mair V. (2017) A petrographic study of carbonate phases in the Ulten Zone ultramafic rocks: Insights into carbonation in the mantle wedge and exhumation-related decarbonation. *Ofioliti* **42**, 105–127.

Frezzotti M. L., Selverstone J., Sharp Z. D. and Compagnoni R. (2011) Carbonate dissolution during subduction revealed by diamond-bearing rocks from the Alps. *Nat. Geosci.* **4**, 703–706.

Früh-Green G. L., Kelley D. S., Bernasconi S. M., Karson J. A., Ludwig K. A., Butterfield D. A., Boschi C. and Proskurowski G. (2003) 30000 years of hydrothermal activity at the Lost City vent field. *Nature* **301**, 495–498.

Fryer P., Wheat C. G., Williams T., Kelley C., Johnson K., Ryan J., Kurz W., Shervais J., Albers E., Bekins B., Debret B., Deng J., Dong Y., Eickenbusch P., Frery E., Ichiyama Y., Johnston R., Kevorkian R., Magalhaes V., Mantovanelli S., Menapace W., Menzies C., Michibayashi K., Moyer C., Mullane K., Park J.-W., Price R., Sissmann O., Suzuki S., Takai K., Walter B., Zhang R., Amon D., Glickson D. and Pomponi S. (2020) Mariana serpentinite mud volcanism exhumes subducted seamount materials: implications for the origin of life. *Phil. Trans. R. Soc. A* **378**, 20180425.

Fukui H., Ohtaka O., Fujisawa T., Kunisada T., Suzuki T. and Kikegawa T. (2003) Thermo-elastic property of $Ca(OH)_2$ portlandite. *High Pressure Res.* **23**, 55–61.

Galvez M. E. and Pubellier M. (2019) How do subduction zones regulate the carbon cycle? In *Deep carbon: Past to Present* (eds. B. N. Orcutt, I. Daniel and R. Dasgupta). Cambridge University Press, Cambridge. pp. 276–312.

Galvez M. E., Beyssac O., Martinez I., Benzerara K., Chaduteau C., Malvoisin B. and Malavieille J. (2013a) Graphite formation by carbonate reduction during subduction. *Nat. Geosci.* **6**, 473–477.

Galvez M. E., Martinez I., Beyssac O., Benzerara K., Agrinier P. and Assayag N. (2013b) Metasomatism and graphite formation at a lithological interface in Malaspina (Alpine Corsica, France). *Contrib. Mineral. Petrol.* **166**, 1687–1708.

Giuntoli F., Vitale Brovarone A. and Menegon L. (2020) Feedback between high-pressure genesis of abiotic methane and strain localization in subducted carbonate rocks. *Sci. Rep.* **10**, 9848.

Goldstein R. H. and Reynolds T. J. (1994) *Systematics of fluid inclusions in diagenetic minerals*. SEPM (Society for Sedimentary Geology) Short Course 31, Tulsa.

Grozeva N. G., Klein F., Seewald J. S. and Sylva S. P. (2017) Experimental study of carbonate formation in oceanic peridotite. *Geochim. Cosmochim. Acta* **199**, 264–286.

Grozeva N. G., Klein F., Seewald J. S. and Sylva S. P. (2020) Chemical and isotopic analyses of hydrocarbon-bearing fluid inclusions in olivine-rich rocks. *Phil. Trans. R. Soc. A* **378**, 20180431.

Guillot S., Schwartz S., Reynard B., Agard P. and Prigent C. (2015) Tectonic significance of serpentinites. *Tectonophysics* **646**, 1–19.

Hayes J. M. and Waldbauer J. R. (2006) The carbon cycle and associated redox processes through time. *Phil. Trans. R. Soc. B* **361**, 931–950.

Hoefs J. (2009) *Stable Isotope Geochemistry, 6th ed*. Springer-Verlag, Berlin Heidelberg.

Holland T. J. B. and Powell R. (1998) An internally consistent thermodynamic data set for phases of petrological interest. *J. Metamorph. Geol.* **16**, 309–343.

Holloway J. R. (1984) Graphite–CH_4–H_2O–CO_2 equilibria at low-grade metamorphic conditions. *Geology* **12**, 455–458.

Hu Z., Liu Y., Gao S., Xiao S., Zhao L., Günther D., Li M., Zhang W. and Zong K. (2012) A "wire" signal smoothing device for laser ablation inductively coupled plasma mass spectrometry analysis. *Spectrochim. Acta B* **78**, 50–57.

Hu H., Vitale Brovarone A., Zhang L., Piccoli F., Peng W. and Shen T. (2021) Retrograde carbon sequestration in orogenic complexes: A case study from the Chinese southwestern Tianshan. *Lithos* **392–393**, 106151.

Huang F., Daniel I., Cardon H., Montagnac G. and Sverjensky D. A. (2017) Immiscible hydrocarbon fluids in the deep carbon cycle. *Nat. Commun.* **8**, 15798.

Jaeckel K., Bebout G. E. and Angiboust S. (2018) Deformation-enhanced fluid and mass transfer along Western and Central Alps paleo-subduction interfaces: Significance for carbon cycling models. *Geosphere* **14**, 2355–2375.

Johannes W. and Puhan D. (1971) The calcite-aragonite transition, reinvestigated. *Contrib. Mineral. Petrol.* **31**, 28–38.

Kelemen P. B. and Manning C. E. (2015) Reevaluating carbon fluxes in subduction zones, what goes down, mostly comes up. *Proc. Natl. Acad. Sci. USA* **112**, E3997–E4006.

Kelley D. S., Karson J. A., Blackman D. K., Früh-Green G. L., Butterfield D. A., Lilley M. D., Olson E. J., Schrenk M. O., Roe K. K., Lebon G. T., Rivizzigno P. and the AT3-60 Shipboard Party. (2001) An off-axis hydrothermal vent field near the Mid-Atlantic Ridge at 30° N. *Nature* **412**, 145–149.

Kelley D. S., Karson J. A., Früh-Green G. L., Yoerger D. R., Shank T. M., Butterfield D. A., Hayes J. M., Schrenk M. O., Olson E. J., Proskurowski G., Jakuba M., Bradley A., Larson B., Ludwig K., Glickson D., Buckman K., Bradley A. S., Brazelton W. J., Roe K., Elend M. J., Delacour A., Bernasconi

S. M., Lilley M. D., Baross J. A., Summons R. E. and Sylva S. P. (2005) A serpentinite-hosted ecosystem: The Lost City hydrothermal field. *Science* **307**, 1428–1434.

Klein F., Bach W. and McCollom T. M. (2013) Compositional controls on hydrogen generation during serpentinization of ultramafic rocks. *Lithos* **178**, 55–69.

Klein F., Humphris S. E., Guo W., Schubotz F., Schwarzenbach E. M. and Orsi W. D. (2015) Fluid mixing and the deep biosphere of a fossil Lost City-type hydrothermal system at the Iberia Margin. *Proc. Natl. Acad. Sci. USA* **112**, 12036–12041.

Klein F., Grozeva N. G. and Seewald J. S. (2019) Abiotic methane synthesis and serpentinization in olivine-hosted fluid inclusions. *Proc. Natl. Acad. Sci. USA* **116**, 17666–17672.

Klein F., Tarnas J. D. and Bach W. (2020) Abiotic sources of molecular hydrogen on Earth. *Elements* **16**, 19–24.

Lafay R., Baumgartner L. P., Stephane S., Suzanne P., German M. H. and Torsten V. (2017) Petrologic and stable isotopic studies of a fossil hydrothermal system in ultramafic environment (Chenaillet ophicalcites, Western Alps, France): Processes of carbonate cementation. *Lithos* **294–295**, 319–338.

Lamadrid H. M., Rimstidt J. D., Schwarzenbach E. M., Klein F., Ulrich S., Dolocan A. and Bodnar R. J. (2017) Effect of water activity on rates of serpentinization of olivine. *Nat. Commun.* **8**, 16107.

Lamadrid H. M., Zajacz Z., Klein F. and Bodnar R. J. (2021) Synthetic fluid inclusions XXIII. Effect of temperature and fluid composition on rates of serpentinization of olivine. *Geochim. Cosmochim. Acta* **292**, 285–308.

Lazar C. (2020) Using silica activity to model redox-dependent fluid compositions in serpentinites from 100 to 700 ^{o}C and from 1 to 20 kbar. *J. Petrol.* **61**, egaa101.

Lazar C., Zhang C., Manning C. E. and Mysen B. O. (2014) Redox effects on calcite–portlandite–fluid equilibria at forearc conditions: Carbon mobility, methanogenesis, and reduction melting of calcite. *Am. Mineral.* **99**, 1604–1615.

Li Y. (2017) Immiscible C–H–O fluids formed at subduction zone conditions. *Geochem. Perspect. Lett.* **3**, 12–21.

Li X.-P., Zhang L., Wei C., Ai Y. and Chen J. (2007) Petrology of rodingite derived from eclogite in western Tianshan, China. *J. Metamorph. Geol.* **25**, 363–382.

Li X.-P., Zhang L.-F., Wilde S. A., Song B. and Liu X.-M. (2010) Zircons from rodingite in the Western Tianshan serpentinite complex: mineral chemistry and U–Pb ages define nature and timing of rodingitization. *Lithos* **118**, 17–34.

Li J.-L., Klemd R., Gao J. and Meyer M. (2012) Coexisting carbonate-bearing eclogite and blueschist in SW Tianshan, China: Petrology and phase equilibria. *J. Asian Earth Sci.* **60**, 174–187.

Li J.-L., Klemd R., Gao J. and Meyer M. (2014) Compositional zoning in dolomite from lawsonite-bearing eclogite (SW Tianshan, China): Evidence for prograde metamorphism during subduction of oceanic crust. *Am. Mineral.* **99**, 206–217.

Li X., Zhang L., Wei C., Slabunov A. I. and Bader T. (2018) Quartz and orthopyroxene exsolution lamellae in clinopyroxene and the metamorphic *P–T* path of Belomorian eclogites. *J. Metamorph. Geol.* **36**, 1–22.

Lin F., Bodnar R. J. and Becker S. P. (2007) Experimental determination of the Raman CH_4 symmetric stretching ($\gamma 1$) band position from 1–650 bar and 0.3–22 ^{o}C: Application to fluid inclusion studies. *Geochim. Cosmochim. Acta* **71**, 3746–3756.

Lin M., Zhang G., Li N., Li H. and Wang J. (2021) An improved *in situ* zircon U–Pb dating method at high spatial resolution (≤ 10 μm spot) by LA-MC-ICP-MS and its application. *Geostand. Geoanal. Res.* **45**, 265–285.

Liou J. G., Tsujimori T., Zhang R. Y., Katayama I. and Maruyama S. (2004) Global UHP metamorphism and continental subduction/collision: the Himalayan model. *Int. Geol. Rev.* **46**, 1–27.

Lü Z. and Zhang L. (2012) Coesite in the eclogite and schist of the Atantayi Valley, southwestern Tianshan, China. *Chinese Sci. Bull.* **57**, 1467–1472.

Lü Z., Bucher K., Zhang L. and Du J. (2012a) The Habutengsu metapelites and metagreywackes in western Tianshan, China: metamorphic evolution and tectonic implications. *J. Metamorph. Geol.* **30**, 907–926.

Lü Z., Zhang L., Du J., Yang X., Tian Z. and Xia B. (2012b) Petrology of HP metamorphic veins in coesite-bearing eclogite from western Tianshan, China: Fluid processes and elemental mobility during exhumation in a cold subduction zone. *Lithos* **136–139**, 168–186.

Malvoisin B., Chopin C., Brunet F. and Galvez M. E. (2012) Low-temperature wollastonite formed by carbonate reduction: a marker of serpentinite redox conditions. *J. Petrol.* **53**, 159–176.

McCollom T. M. and Bach W. (2009) Thermodynamic constraints on hydrogen generation during serpentinization of ultramafic rocks. *Geochim. Cosmochim. Acta* **73**, 856–875.

McCollom T. M. and Seewald J. S. (2001) A reassessment of the potential for reduction of dissolved CO_2 to hydrocarbons during serpentinization of olivine. *Geochim. Cosmochim. Acta* **65**, 3769–3778.

McCollom T. M. and Seewald J. S. (2013) Serpentinites, hydrogen, and life. *Elements* **9**, 129–134.

McDermott J. M., Seewald J. S., German C. R. and Sylva S. P. (2015) Pathways for abiotic organic synthesis at submarine hydrothermal fields. *Proc. Natl. Acad. Sci. USA* **112**, 7668–7672.

Ménez B. (2020) Abiotic hydrogen and methane: Flues for life. *Elements* **16**, 39–46.

Mukhina E., Kolesnikov A. and Kutcherov V. (2017) The lower pT limit of deep hydrocarbon synthesis by $CaCO_3$ aqueous reduction. *Sci. Rep.* **7**, 5749.

Peng W., Zhang L., Shen T. and Hu H. (2018) Implications for the deep carbon cycle from the carbonation in subduction zones: A case study of carbonated micaschists from Chinese southwestern Tianshan. *Acta Petrol. Sin.* **34**, 1204–1218.

Peng W., Zhang L., Menzel M. D., Vitale Brovarone A., Tumiati S., Shen T. and Hu H. (2020) Multistage CO_2 sequestration in the subduction zone: Insights from exhumed carbonated serpentinites, SW Tianshan UHP belt, China. *Geochim. Cosmochim. Acta* **270**, 218–243.

Penniston-Dorland S. C., Kohn M. J. and Manning C. E. (2015) The global range of subduction zone thermal structures from exhumed blueschists and eclogites: Rocks are hotter than models. *Earth Planet. Sci. Lett.* **428**, 243–254.

Peretti A., Dubessy J., Mullis J., Frost B. R. and Trommsdorff V. (1992) Highly reducing conditions during Alpine metamorphism of the Malenco peridotite (Sondrio, northern Italy) indicated by mineral paragenesis and H_2 in fluid inclusions. *Contrib. Mineral. Petrol.* **112**, 329–340.

Piccoli F., Vitale Brovarone A., Beyssac O., Martinez I., Ague J. J. and Chaduteau C. (2016) Carbonation by fluid–rock interactions at high-pressure conditions: Implications for carbon cycling in subduction zones. *Earth Planet. Sci. Lett.* **445**, 146–159.

Piccoli F., Vitale Brovarone A. and Ague J. J. (2018) Field and petrological study of metasomatism and high-pressure carbonation from lawsonite eclogite-facies terrains, Alpine Corsica. *Lithos* **304–307**, 16–37.

Plümper O., King H. E., Geisler T., Liu Y., Pabst S., Savov I. P., Rost D. and Zack T. (2017) Subduction zone forearc serpentinites as incubators for deep microbial life. *Proc. Natl. Acad. Sci. USA* **114**, 4324–4329.

Proskurowski G., Lilley M. D., Seewald J. S., Früh-Green, G. L., Olson, E. J., Lupton, J. E., Sylva, S. P. and Kelley, D. S. (2008) Abiogenic hydrocarbon production at Lost City hydrothermal field. *Science* **319**, 604–607.

Ramos F. C., Wolff J. A. and Tollstrup D. L. (2004) Measuring $^{87}Sr/^{86}Sr$ variations in minerals and groundmass from basalts using LA-MC-ICPMS. *Chem. Geol.* **211**, 135–158.

Robie R. A. and Hemingway B. S. (1995) *Thermodynamic properties of minerals and related substances at 298.15 K and 1 bar (10^5 Pascals) pressure and at higher temperatures*. U.S. Geological Survey Bulletin 2131.

Sachan H. K., Mukherjee B. K. and Bodnar R. J. (2007) Preservation of methane generated during serpentinization of upper mantle rocks: Evidence from fluid inclusions in the Nidar ophiolite, Indus Suture Zone, Ladakh (India). *Earth Planet. Sci. Lett.* **257**, 47–59.

Scambelluri M., Müntener O., Ottolini L., Pettke T. T. and Vannucci R. (2004) The fate of B, Cl and Li in the subducted oceanic mantle and in the antigorite breakdown fluids. *Earth Planet. Sci. Lett.* **222**, 217–234.

Scambelluri M., Bebout G. E., Belmonte D., Gilio M., Campomenosi N., Collins N. and Crispini L. (2016) Carbonation of subduction-zone serpentinite (high-pressure ophicarbonate; Ligurian Western Alps) and implications for the deep carbon cycling. *Earth Planet. Sci. Lett.* **441**, 155–166.

Schwarzenbach E. M., Früh-Green G. L., Bernasconi S. M., Alt J. C. and Plas A. (2013) Serpentinization and carbon sequestration: A study of two ancient peridotite-hosted hydrothermal systems. *Chem. Geol.* **351**, 115–133.

Scicchitano M. R., Rubatto D., Hermann J., Shen T., Padrón-Navarta J. A., Williams I. S. and Zheng Y.-F. (2018) *In situ* oxygen isotope determination in serpentine minerals by ion microprobe: reference materials and applications to ultrahigh-pressure serpentinites. *Geostand. Geoanal. Res.* **42**, 459–479.

Sharma A., Cody G. D. and Hemley R. J. (2009) *In situ* diamond-anvil cell observations of methanogenesis at high pressures and temperatures. *Energ. Fuel.* **23**, 5571–5579.

Sheik C. S., Cleaves II H. J., Johnson-Finn K., Giovannelli D., Kieft T. L., Papineau D., Schrenk M. O. and Tumiati S. (2020) Abiotic and biotic processes that drive carboxylation and decarboxylation reactions. *Am. Mineral.* **105**, 609–615.

Shen T., Zhang L. and Li X. (2012) Geochemical characteristics of rodingite derived from eclogite in western Tianshan, Xinjiang, China and its implications for subduction zone fluid. *Acta Petrol. Sin.* **28**, 2235–2249.

Shen T., Hermann J., Zhang L., Lü Z., Padrón-Navarta J. A., Xia B. and Bader T. (2015) UHP metamorphism documented in Ti-chondrodite- and Ti-clinohumite-bearing serpentinized ultramafic rocks from Chinese southwestern Tianshan. *J. Petrol.* **56**, 1425–1458.

Shen T., Wu F., Zhang L., Hermann J., Li X. and Du J. (2016) In-situ U–Pb dating and Nd isotopic analysis of perovskite from a rodingite blackwall associated with UHP serpentinite from southwestern Tianshan, China. *Chem. Geol.* **431**, 67–82.

Shi G. U., Tropper P., Cui W., Tan J. and Wang C. (2005) Methane (CH_4)-bearing fluid inclusions in the Myanmar jadeitite. *Geochem. J.* **39**, 503–516.

Sieber M. J., Hermann J. and Yaxley G. M. (2018) An experimental investigation of C–O–H fluid-driven carbonation of serpentinites under forearc conditions. *Earth Planet. Sci. Lett.* **496**, 178–188.

Sieber M. J., Yaxley G. M. and Hermann J. (2020) Investigation of fluid-driven carbonation of a hydrated, forearc mantle wedge using serpentinite cores in high-pressure experiments. *J. Petrol.* **61**, egaa035.

Song S., Su L., Niu Y., Lai Y. and Zhang L. (2009) CH_4 inclusions in orogenic harzburgite: Evidence for reduced slab fluids and implication for redox melting in mantle wedge. *Geochim. Cosmochim. Acta* **73**, 1737–1754.

Steele-MacInnis M., Lecumberri-Sanchez P. and Bodnar R. J. (2012) HOKIEFLINCS_H_2O-NaCl: A Microsoft Excel spreadsheet for interpreting microthermometric data from fluid inclusions based on the *PVTX* properties of H_2O–NaCl. *Comput. Geosci.* **49**, 334–337.

Syracuse E. M., van Keken P. E. and Abers G. A. (2010) The global range of subduction zone thermal models. *Phys. Earth Planet. In.* **183**, 73–90.

Tan Z., Agard P., Gao J., John T., Li J., Jiang T., Bayet L., Wang X. and Zhang X. (2017) P–T–time-isotopic evolution of coesite-bearing eclogites: Implications for exhumation processes in SW Tianshan. *Lithos* **278–281**, 1–25.

Tao R., Zhang L., Fei Y. and Liu Q. (2014) The effect of Fe on the stability of dolomite at high pressure: Experimental study and petrological observation in eclogite from southwestern Tianshan, China. *Geochim. Cosmochim. Acta* **143**, 253–267.

Tao R., Zhang L., Tian M., Zhu J., Liu X., Liu J., Höfer H. E., Stagno V. and Fei Y. (2018a) Formation of abiotic hydrocarbon from reduction of carbonate in subduction zones: Constraints from petrological observation and experimental simulation. *Geochim. Cosmochim. Acta* **239**, 390–408.

Tao R., Zhang L., Li S., Zhu J. and Ke S. (2018b) Significant contrast in the Mg-C-O isotopes of carbonate between carbonated eclogite and marble from the S.W. Tianshan UHP subduction zone: Evidence for two sources of recycled carbon. *Chem. Geol.* **483**, 65–77.

Tian Z. L. and Wei C. J. (2013) Metamorphism of ultrahigh-pressure eclogites from the Kebuerte Valley, South Tianshan, NW China: phase equilibria and *P–T* path. *J. Metamorph. Geol* **31**, 281–300.

Truche L., McCollom T. M. and Martinez I. (2020) Hydrogen and abiotic hydrocarbons: Molecules that change the world. *Elements* **16**, 13–18.

Tumiati S. and Malaspina N. (2019) Redox processes and the role of carbon-bearing volatiles from the slab–mantle interface to the mantle wedge. *J. Geol. Soc.* **176**, 388–397.

Tumiati S., Fumagalli P., Tiraboschi C. and Poli S. (2013) An experimental study on COH-bearing peridotite up to 3.2 GPa and implications for crust–mantle recycling. *J. Petrol.* **54**, 453–479.

Tumiati S., Tiraboschi C., Sverjensky D. A., Pettke T., Recchia S., Ulmer P., Miozzi F. and Poli S. (2017) Silicate dissolution boosts the CO_2 concentrations in subduction fluids. *Nat. Commun.* **8**, 616.

Tumiati S., Tiraboschi C., Miozzi F., Vitale-Brovarone A., Manning C. E., Sverjensky D. A., Milani S. and Poli S. (2020) Dissolution susceptibility of glass-like carbon versus crystalline graphite in high-pressure aqueous fluids and implications for the behavior of organic matter in subduction zones. *Geochim. Cosmochim. Acta* **273**, 383–402.

Ueno Y., Yamada K., Yoshida N., Maruyama S. and Isozaki Y. (2006) Evidence from fluid inclusions for microbial methanogenesis in the early Archaean era. *Nature* **440**, 516–519.

van der Straaten F., Halama R., John T., Schenk V., Hauff F. and Andersen N. (2012) Tracing the effects of high-pressure metasomatic fluids and seawater alteration in blueschist-facies overprinted eclogites: Implications for subduction channel processes. *Chem. Geol.* **292–293**, 69–87.

Veizer J., Ala D., Azmy K., Bruckschen P., Buhl D., Bruhn F., Carden G. A. F., Diener A., Ebneth S., Godderis Y., Jasper T., Korte C., Pawellek, F., Podlaha O. G. and Strauss H. (1999) $^{87}Sr/^{86}Sr$, $\delta^{13}C$ and $\delta^{18}O$ evolution of Phanerozoic seawater. *Chem. Geol.* **161**, 59–88.

Vitale Brovarone A., Martinez I., Elmaleh A., Compagnoni R., Chaduteau C., Ferraris C. and Esteve I. (2017) Massive production of abiotic methane during subduction evidenced in metamorphosed ophicarbonates from the Italian Alps. *Nat. Commun.* **8**, 14134.

Vitale Brovarone A., Sverjensky D. A., Piccoli F., Ressico F., Giovannelli D. and Daniel I. (2020) Subduction hides high-pressure sources of energy that may feed the deep subsurface biosphere. *Nat. Commun.* **11**, 3880.

Vroon P. Z., van der Wagt B., Koornneef J. M. and Davies G. R. (2008) Problems in obtaining precise and accurate Sr isotope analysis from geological materials using laser ablation MC-ICPMS. *Anal. Bioanal. Chem.* **390**, 465–476.

Wheat C. G., Seewald J. S. and Takai K. (2020) Fluid transport and reaction processes within a serpentinite mud volcano: South Chamorro Seamount. *Geochim. Cosmochim. Acta* **269**, 413–428.

Whitney D. L. and Evans B. W. (2010) Abbreviations for names of rock-forming minerals. *Am. Mineral.* **95**, 185–187.

Woodhead J., Swearer S., Hergt J. and Maas R. (2005) *In situ* Sr-isotope analysis of carbonates by LA-MC-ICP-MS: interference corrections, high spatial resolution and an example from otolith studies. *J. Anal. At. Spectrom.* **20**, 22–27.

Xia B., Zhang L., Xia Y. and Bader T. (2014) The tectonic evolution of the Tianshan Orogenic Belt: Evidence from U–Pb dating of detrital zircons from the Chinese southwestern Tianshan accretionary mélange. *Gondwana Res.* **25**, 1627–1643.

Xu H., Zhao Y., Vogel S. C., Daemen L. L. and Hickmott D. D. (2007) Anisotropic thermal expansion and hydrogen bonding behavior of portlandite: A high-temperature neutron diffraction study. *J. Solid State Chem.* **180**, 1519–1525.

Yang Y., Wu F., Xie L., Yang J. and Zhang Y. (2009) In-situ Sr isotopic measurement of natural geological samples by LA-MC-ICP-MS. *Acta Petrol. Sin.* **25**, 3431–3441.

Yang C., Ni Z., Wang T., Chen Z., Hong H., Wen L., Luo B. and Wang W. (2018) A new genetic mechanism of natural gas accumulation. *Sci. Rep.* **8**, 8336.

Zhang L., Du J., Lü Z., Yang X., Gou L., Xia B., Chen Z., Wei C. and Song S. (2013) A huge oceanic-type UHP metamorphic belt in southwestern Tianshan, China: Peak metamorphic age and *P–T* path. *Chinese Sci. Bull.* **58**, 4378–4383.

Zhang L., Wang Y., Zhang L. and Lü Z. (2019) Ultrahigh pressure metamorphism and tectonic evolution of southwestern Tianshan orogenic belt, China: a comprehensive review. In *HP–UHP Metamorphism and Tectonic Evolution of Orogenic Belts* (eds. L. Zhang, Z. Zhang, H.-P. Schertl and C. Wei). Geological Society, London, Special Publications. pp. 133–152.

Zhang L., Wang Q., Ding X. and Li W.-C. (2021) Diverse serpentinization and associated abiotic methanogenesis within multiple types of olivine-hosted fluid inclusions in orogenic peridotite from northern Tibet. *Geochim. Cosmochim. Acta* **296**, 1–17.

Zhu J., Zhang L., Lü Z. and Bader T. (2018) Elemental and isotopic (C, O, Sr, Nd) compositions of Late Paleozoic carbonated eclogite and marble from the SW Tianshan UHP belt, NW China: Implications for deep carbon cycle. *J. Asian Earth Sci.* **153**, 307–324.

Zhu J., Zhang L., Tao R. and Fei Y. (2020) The formation of graphite-rich eclogite vein in S.W. Tianshan (China) and its implication for deep carbon cycling in subduction zone. *Chem. Geol.* **533**, 119430.

FIGURE CAPTIONS

Fig. 1. Geological background of the Chinese southwestern Tianshan. (A) Simplified tectonic framework of the western part of the Chinese Tianshan (modified from Tian and Wei, 2013). (B) Schematic geological map of the Chinese southwestern Tianshan H*P*–UH*P* metamorphic belt (modified from Zhang et al., 2013). Grey stars show sample localities of CH_4-bearing carbonated eclogites at Kebuerte and Habutengsu in the metamorphic belt (Tao et al., 2018a). (C) Detailed geological map of Changawuzi showing the sample locality of CH_4-bearing ophidolomites in this study (modified from Shen et al., 2015).

Fig. 2. Petrological characteristics of the studied ophidolomites. (A and B) Discontinuous and folded dolomite veins (with the rim encircled by yellowish calcite and brucite) filling the host serpentinites (hand-specimen scale). (C and D) Dolomite growth at the expense of antigorite, with unreacted antigorite visible (cross-polarized light). In some cases, antigorite shows abnormal interference colors due to the thick sections. (E and F) Decomposition of dolomite into cloudy calcite and brucite (cross-polarized light). (G) Back-scattered electron image (the upper part) and compositional X-ray map (the lower part) of dolomite decomposition into calcite–brucite intergrowths. The newly grown calcite and brucite extend into the inner parts of dolomite along microcracks. (H) The enlargement of the box in (G) showing intergrowths of acicular calcite and brucite and patches of relict dolomite in calcite. Mineral abbreviations in this study follow Whitney and Evans (2010).

Fig. 3. Occurrence of olivine and microstructures of magnetite-hosted mineral inclusions in the studied ophidolomites. (A) Olivine relicts in the antigorite matrix. (B) Coarse magnetite grains enclosing abundant minerals in the matrix of antigorite and dolomite. (C) Olivine in association with antigorite and brucite in magnetite. (D) Calcite and brucite growth at the expense of dolomite in magnetite, with dolomite relicts visible.

Fig. 4. Petrographic characteristics of fluid inclusions in the studied ophidolomites. (A and B) Type-I two-phase (vapor and liquid) fluid inclusions in dolomite. (C and D) Type-II single-phase fluid inclusions in dolomite. (E–G) Type-I two-phase (vapor and liquid) fluid inclusions in calcite intergrown with brucite.

Fig. 5. Raman spectra of fluid inclusions in the studied ophidolomites. (A and B) Type-I CH_4-bearing aqueous fluid inclusions in dolomite (A) and calcite intergrown with brucite (B). The strong fluorescence of the host carbonates sometimes prevents conclusive Raman investigation of the liquid phase of H_2O. (C) Type-II $CH_4 \pm H_2$-bearing fluid inclusions in dolomite. Weaker but crucial peaks are enlarged. Scale bars of the close-up images are 10 μm.

Fig. 6. Isotope compositions of the studied ophidolomites. (A) *In situ* Sr isotope compositions of dolomite and calcite. The sky blue and purple dashed lines show $^{87}Sr/^{86}Sr$ ratios of the Tianshan H*P* ophidolomites and their dolomite separates (Peng et al., 2020) and the Ordovician–Carboniferous seawater (Veizer et al., 1999), respectively. The Tianshan UH*P* serpentinites are marine-originated (Shen et al., 2015) and have largely inherited Sr isotope compositions of the seawater (Peng et al., 2020). The sky blue and purple solid lines show the average $^{87}Sr/^{86}Sr$ ratios of dolomite and calcite, respectively. Error bars represent the 2σ internal precision. (B) C and O isotope compositions of dolomite and calcite. For comparison, $\delta^{13}C$ and $\delta^{18}O$ of carbonates in various lithologies from the Chinese southwestern Tianshan are plotted (van der Straaten et al., 2012; Collins et al., 2015; Peng et al., 2018, 2020; Zhu et al., 2018). The green and grey areas display $\delta^{13}C$ of marine carbonates (Hoefs, 2009) and carbonates in CH_4-bearing ophicalcites from the Western Alps (Vitale Brovarone et al., 2017), respectively. The black and blue solid lines correspond to C isotopic trends of carbonates affected by decarbonation and carbonate reduction from Galvez et al. (2013b), while the black and blue dashed lines represent the possible trends of decarbonation and carbonate reduction in the Tianshan. Uncertainties of values are smaller than the symbol sizes.

Fig. 7. (A) Stabilities of phases under variable fO_2–fH_2 conditions in the Ca–Mg–C–O–H system (with fixed Ca:Mg:C of 1:1:2 in molar ratio) at 8 kbar and 420 °C.

The orange dashed lines show log fO_2 of magnetite–hematite (MH), fayalite–magnetite–quartz (FMQ), and iron–magnetite (IM) buffers calculated at 8 kbar and 420 °C. The pink solid line represents the thermodynamically calculated model of slightly reduced H_2O at X_O = 0.33 ~ 1/3 in the H–O system (star: X_O = 0.3333323, corresponding to y_{H2O} = 0.999995 and y_{H2} = 0.000005). (B) The *P*–*T* pseudosection displaying diverse phase assemblages in the Ca–Fe–Mg–Si–C–O–H system at log fO_2 = –26.0 and log fH_2 = 0.8. The rectangle confines *P*–*T* conditions for the onset of retrograde serpentinization in the Tianshan (7–9 kbar and 410–430 °C; Li et al., 2007, 2010).

Fig. 8. *P*–*T* diagram showing stages of dolomite reduction and fluid entrapment during exhumation of the Chinese southwestern Tianshan. Stage A represents the onset of dolomite reduction, inferred from retrograde serpentinization starting at 7–9 kbar and 410–430 °C and propagating to lower *P*–*T* conditions (Stage B) in the Tianshan (Li et al., 2007, 2010). Solid lines marked with 1, 2, and 3 display the controversial *P*–*T* conditions for the chrysotile to antigorite transition from Li et al. (2007, 2010), Scambelluri et al. (2004), and Evans et al. (1976), respectively, resulting in uncertainties of Stage B. The constrained *P*–*T* conditions for fluid entrapment (Stage C) are based on the fluid inclusion isochores intersecting the retrograde *P*–*T* path of the Tianshan (Tan et al., 2017). The stability fields of lizardite, antigorite, and olivine, as well as the main transformation reactions and cold subduction gradient, are from Guillot et al. (2015). The calcite to aragonite transition is from Johannes and Puhan (1971).

Fig. 9. (A) Summary of abiotic CH_4 formation through dolomite reduction in ophidolomites during exhumation of the Chinese southwestern Tianshan. The *P*–*T* constraints for H*P* ophidolomites in the Tianshan are from Peng et al. (2020). The red rectangle [T] displays *P*–*T* conditions for the onset of dolomite reduction, inferred from retrograde serpentinization in the Tianshan (Li et al., 2007, 2010).

For comparison, *P–T* estimates for carbonate reduction during shallow subduction in Alpine Corsica [C] (Malvoison et al., 2012; Galvez et al., 2013a, b) and the Italian Alps [A] (Vitale Brovarone et al., 2017; Giuntoli et al., 2020) are shown. The *P–T* path of the Tianshan is from Tan et al. (2017). The cyan and light cyan areas represent the modelled prograde *P–T* paths of subduction zones at the slab interface and slab Moho (7 km beneath the slab surface; Syracuse et al., 2010), respectively. The sky blue solid curve (PD) shows the global average range of prograde *P–T* paths from subduction-related metamorphic rocks (Penniston-Dorland et al., 2015). Facies boundaries and abbreviations are from Liou et al. (2004). (B) General model showing abiotic CH_4 production through dolomite reduction during shallow subduction. Due to uncertainties in the scale and extent of serpentinization in subducted slabs (Li et al., 2007, 2010; Vitale Brovarone et al., 2017, 2020; Lazar, 2020), dashed arrow lines represent fluid migration pathways instead of the steady fluid flow. The extent of alteration is dependent on the infiltration of the reactive reduced fluids. Possible CH_4–H_2-generating reactions are listed but without stoichiometric numbers. Figure is not to scale.

Table 1. Representative bulk-rock compositions of the studied ophidolomite (Sample C1534).

Sample	SiO_2	TiO_2	Al_2O_3	Fe_2O_3	FeO	MnO	MgO	CaO	Na_2O	K_2O	P_2O_5	LOI		Total
XRF analysis (wt%)														
C1534	13.20	0.01	0.18	1.78	1.36	0.32	26.47	20.69	0.01	0.06	0.04	35.31		99.43
Effective bulk-rock composition derived from mineral compositions and														

modes (wt%)														
	SiO_2	TiO_2	Al_2O_3	Fe_2O_3	FeO	MnO	MgO	CaO	Na_2O	K_2O	P_2O_5	H_2O	CO_2	
C1534	13.28	—	0.09	1.28	1.73	0.30	26.92	20.96	—	—	—	4.42	31.02	100.00

Table 2. Representative mineral compositions of the studied ophidolomites

Sample	C1534	CP1734								
Mineral	Atg	Dol	Cal	Brc	Mag	Ol	Atg	Dol	Cal	Brc
SiO_2	44.31	0.00	0.00	0.12	0.00	41.76	44.44	0.00	0.00	0.01
TiO_2	0.00	0.00	0.00	0.00	0.10	0.02	0.00	0.00	0.04	0.04
Al_2O_3	0.29	0.00	0.00	0.01	0.00	0.02	0.51	0.00	0.00	0.00
Cr_2O_3	0.03	0.00	0.00	0.01	0.00	0.01	0.03	0.00	0.00	0.00
Fe_2O_3	n.d.	n.d.	n.d.	n.d.	n.d.	n.d.	n.d.	n.d.	n.d.	n.d.
FeO	2.43	0.64	0.00	2.54	91.25	6.59	2.21	0.68	0.04	2.09
MnO	0.00	0.49	0.16	0.42	0.35	0.63	0.03	0.24	0.12	0.57
MgO	40.03	21.77	0.09	79.94	0.68	51.40	40.33	21.91	0.19	75.50
CaO	0.02	32.23	59.48	0.52	0.02	0.04	0.01	32.39	60.09	0.24
Na_2O	0.00	0.00	0.00	0.00	0.00	0.00	0.01	0.00	0.00	0.03
K_2O	0.02	0.00	0.00	0.00	0.02	0.02	0.01	0.01	0.00	0.01
Total	87.13	55.13	59.73	83.56	92.42	100.49	87.58	55.23	60.48	78.49
Si	34.058	0.000	0.000	0.001	0.000	1.003	33.928	0.000	0.000	0.000
Ti	0.000	0.000	0.000	0.000	0.003	0.000	0.000	0.000	0.001	0.000
Al	0.263	0.000	0.000	0.000	0.000	0.001	0.459	0.000	0.000	0.000
Cr	0.018	0.000	0.000	0.000	0.000	0.000	0.018	0.000	0.000	0.000
Fe^{3+}	n.c.	0.000	0.000	0.000	1.995	0.000	n.c.	0.000	0.000	0.000
Fe^{2+}	1.562	0.016	0.000	0.017	0.950	0.132	1.411	0.017	0.001	0.015
Mn	0.000	0.012	0.004	0.003	0.011	0.013	0.019	0.006	0.003	0.004
Mg	45.869	0.955	0.004	0.974	0.039	1.840	45.903	0.958	0.009	0.977
Ca	0.016	1.017	1.992	0.005	0.001	0.001	0.008	1.019	1.986	0.002
Na	0.000	0.000	0.000	0.000	0.000	0.000	0.015	0.000	0.000	0.001
K	0.020	0.000	0.000	0.000	0.001	0.001	0.010	0.000	0.000	0.000
Cation	82	2	2	1	3	3	82	2	2	1
O	116	0	0	2	4	4	116	0	0	2
X_{Mg}	0.967	0.984	–	0.982	–	0.933	0.970	0.983	–	0.985

X_{Mg} = Mg/(Mg + Fe); n.d. = not determined; n.c. = not calculated

Table 3. Microthermometric data of representative dolomite-hosted Type-I FIAs in the studied ophidolomites

Table 4. Representative Sr isotope compositions of dolomite and calcite in the studied ophidolomites.

Sample	^{88}Sr (V)	^{85}Rb (mV)	$^{87}Rb/^{86}Sr$	2σ	$^{87}Sr/^{86}Sr$	2σ
Dolomite						
C1534-B2-1-1	1.10	0.01	0.00005	0.00003	0.70524	0.00013

Sample	FIA	Number of analyses	Average T_m (°C)	Average T_h (°C)	Average salinity (wt% NaCl)	Average P_h (bar)	Average dP/dT (bar/°C)
C1534	1	6	–3.6	204.8	5.9	16	15.7
	2	3	–3.2	231.0	5.3	27	14.2
	3	4	–2.4	227.4	4.0	26	14.3
CP1734	1	5	–3.4	178.5	5.6	9	17.0
	2	5	–2.5	183.9	4.2	11	16.5
	3	4	–1.3	191.4	2.2	13	16.0

C1534-B2-1-2	1.38	0.02	0.00005	0.00003	0.70592	0.00011
C1534-B2-1-3	1.40	0.03	0.00006	0.00003	0.70585	0.00013
C1534-B2-2-1	1.18	0.06	0.00017	0.00003	0.70552	0.00012
C1534-B2-2-2	1.02	0.02	0.00007	0.00003	0.70554	0.00014
C1534-B2-2-3	1.13	0.05	0.00015	0.00003	0.70554	0.00013
C1534-B2-3-1	1.08	0.02	0.00005	0.00003	0.70496	0.00013
C1534-B2-3-2	1.52	0.05	0.00010	0.00002	0.70528	0.00008
C1534-B2-3-3	1.44	0.02	0.00004	0.00002	0.70572	0.00011
C1534-B2-3-4	2.02	0.01	0.00002	0.00002	0.70515	0.00009
C1534-B2-3-5	1.64	0.05	0.00010	0.00002	0.70542	0.00010
C1534-B2-4-1	1.79	0.04	0.00007	0.00002	0.70511	0.00008
C1534-B2-4-2	1.29	0.02	0.00005	0.00003	0.70534	0.00012
C1534-B2-4-3	1.63	0.06	0.00012	0.00002	0.70548	0.00009
C1534-B2-4-4	1.69	0.05	0.00011	0.00002	0.70515	0.00011
C1534-B2-5-1	1.64	0.06	0.00014	0.00002	0.70496	0.00009
C1534-B2-5-2	1.58	0.06	0.00014	0.00002	0.70509	0.00010
C1534-B2-5-3	1.79	0.04	0.00008	0.00002	0.70518	0.00008
C1534-B2-5-4	1.62	0.03	0.00006	0.00002	0.70527	0.00009
C1534-B2-6-2	1.83	0.02	0.00003	0.00002	0.70525	0.00007

C1534-C1-2-1	1.02	0.03	0.00011	0.00003	0.70590	0.00016
C1534-C1-2-2	1.08	0.04	0.00011	0.00003	0.70633	0.00013
C1534-C1-3-2	1.13	0.01	0.00001	0.00003	0.70683	0.00013
C1534-C1-6-6	1.02	0.03	0.00009	0.00003	0.70575	0.00014
CP1734-a-2-1	1.39	0.03	0.00007	0.00002	0.70705	0.00011
CP1734-a-4-2	0.95	0.02	0.00008	0.00003	0.70654	0.00014
CP1734-a-4-3	0.92	0.08	0.00030	0.00003	0.70721	0.00014
CP1734-d-5-1	0.94	0.02	0.00004	0.00004	0.70588	0.00017
CP1734-d-5-2	1.39	0.04	0.00009	0.00002	0.70757	0.00013
CP1734-d-7-2	0.94	0.04	0.00013	0.00004	0.70614	0.00019
	^{88}Sr (V)	^{85}Rb (mV)	$^{87}Rb/^{86}Sr$	2σ	$^{87}Sr/^{86}Sr$	2σ
Calcite						
C1534-B2-8-2	3.13	0.01	0.00001	0.00001	0.70913	0.00005
C1534-B2-9-3	2.80	0.01	0.00001	0.00001	0.70912	0.00005
C1534-B2-10-1	2.96	0.01	0.00001	0.00001	0.70932	0.00005
C1534-B2-10-2	3.12	0.03	0.00003	0.00001	0.70911	0.00005
C1534-B2-10-3	2.35	0.02	0.00002	0.00001	0.70926	0.00006
C1534-B2-11-1	3.23	0.03	0.00003	0.00001	0.70946	0.00005
C1534-B2-11-2	3.07	0.04	0.00004	0.00001	0.70938	0.00005
C1534-B2-11-3	2.80	0.01	0.00001	0.00001	0.70943	0.00006
C1534-C1-7-1	3.23	0.05	0.00005	0.00001	0.70923	0.00005
C1534-C1-7-2	3.17	0.02	0.00002	0.00001	0.70931	0.00005
C1534-C1-8-1	2.40	0.01	0.00002	0.00001	0.70895	0.00006
C1534-C1-8-2	3.30	0.03	0.00003	0.00001	0.70917	0.00004
C1534-C1-8-3	3.47	0.03	0.00003	0.00001	0.70899	0.00004
C1534-C1-10-1	2.39	0.02	0.00003	0.00001	0.70872	0.00008
CP1734-a-8-3	3.20	0.01	0.00001	0.00001	0.70951	0.00004
CP1734-a-9-1	3.96	0.02	0.00002	0.00001	0.70947	0.00004
CP1734-a-9-2	3.69	0.01	0.00001	0.00001	0.70970	0.00004
CP1734-a-10-1	3.15	0.02	0.00002	0.00001	0.70965	0.00005
CP1734-a-10-3	2.93	0.01	0.00002	0.00001	0.70984	0.00005
CP1734-a-11-1	3.19	0.02	0.00003	0.00001	0.70932	0.00005
CP1734-a-11-3	2.80	0.03	0.00003	0.00001	0.70963	0.00005
CP1734-a-12-1	3.96	0.04	0.00003	0.00001	0.70915	0.00006
CP1734-a-12-2	3.33	0.03	0.00003	0.00001	0.70944	0.00006
CP1734-a-14-1	3.90	0.01	0.00001	0.00001	0.70963	0.00006
CP1734-a-15-1	3.99	0.01	0.00001	0.00001	0.70986	0.00005

CP1734-d-10-1	3.49	0.00	0.00001	0.00001	0.70969	0.00005
CP1734-d-11-1	3.93	0.01	0.00001	0.00001	0.70970	0.00005
CP1734-d-12-2	3.71	0.03	0.00003	0.00001	0.70974	0.00005
CP1734-d-14-1	3.32	0.01	0.00001	0.00001	0.70962	0.00005
CP1734-d-15-1	2.83	0.02	0.00002	0.00001	0.70905	0.00006

Table 5. C and O isotope compositions of dolomite, calcite, and bulk carbonate in the studied ophidolomites

Sample	$\delta^{13}C_{V\text{-}PDB}$	$\delta^{18}O_{V\text{-}SMOW}$	Sample	$\delta^{13}C_{V\text{-}PDB}$	$\delta^{18}O_{V\text{-}SMOW}$
Dolomite			*Calcite*		
C1534-1-1	10.7	9.6	C1534-C-1	9.0	9.5
C1534-1-2	10.5	9.2	C1534-C-2	9.0	10.1
C1534-1-3	10.5	8.7	CP1734-S1-B	7.4	11.4
C1534-2-1	10.0	8.7	CP1734-S2-B	8.2	8.6
C1534-2-2	10.3	8.8	CP1734-S3-B	7.1	8.4
C1534-2-3	10.9	9.3	CP1734-S4-B	8.3	9.0
C1534-3-1	11.3	9.0	CP1734-T1-B	7.1	11.6
C1534-3-2	10.8	9.1	CP1734-T2-B	7.0	11.0
C1534-3-3	11.5	8.1	CP1734-T3-B	7.0	11.9
C1534-4-1	11.2	9.4	CP1734-T4-B	7.5	12.6
C1534-4-2	11.7	8.7	*Bulk carbonate*		
C1534-4-3	10.9	8.5	C1534	10.3	–
C1534-A-2	9.3	8.7	CP1734	8.6	–
C1534-A-4	9.9	8.7			
C1534-B-1	10.8	8.7			
C1534-B-2	11.5	8.4			
C1534-B-3	9.5	8.8			
C1534-B-4	10.9	8.6			
C1534-C-3	11.0	8.6			
C1534-C-4	9.2	8.3			
CP1734-S1-W	11.1	8.3			
CP1734-S2-W	10.8	8.5			
CP1734-S3-W	10.8	8.3			
CP1734-S4-W	10.0	8.7			
CP1734-T2-W	10.1	8.3			
CP1734-T3-W	10.6	8.6			
CP1734-T4-W	10.3	8.8			

Sample	$\delta^{13}C_{V\text{-}PDB}$	$\delta^{18}O_{V\text{-}SMOW}$	Sample	$\delta^{13}C_{V\text{-}PDB}$	$\delta^{18}O_{V\text{-}SMOW}$

Dolomite			*Calcite*		
C1534-1-1	10.7	9.6	C1534-C-1	9.0	9.5
C1534-1-2	10.5	9.2	C1534-C-2	9.0	10.1
C1534-1-3	10.5	8.7	CP1734-S1-B	7.4	11.4
C1534-2-1	10.0	8.7	CP1734-S2-B	8.2	8.6
C1534-2-2	10.3	8.8	CP1734-S3-B	7.1	8.4
C1534-2-3	10.9	9.3	CP1734-S4-B	8.3	9.0
C1534-3-1	11.3	9.0	CP1734-T1-B	7.1	11.6
C1534-3-2	10.8	9.1	CP1734-T2-B	7.0	11.0
C1534-3-3	11.5	8.1	CP1734-T3-B	7.0	11.9
C1534-4-1	11.2	9.4	CP1734-T4-B	7.5	12.6
C1534-4-2	11.7	8.7	*Bulk carbonate*		
C1534-4-3	10.9	8.5	C1534	10.3	–
C1534-A-2	9.3	8.7	CP1734	8.6	–
C1534-A-4	9.9	8.7			
C1534-B-1	10.8	8.7			
C1534-B-2	11.5	8.4			
C1534-B-3	9.5	8.8			
C1534-B-4	10.9	8.6			
C1534-C-3	11.0	8.6			
C1534-C-4	9.2	8.3			
CP1734-S1-W	11.1	8.3			
CP1734-S2-W	10.8	8.5			
CP1734-S3-W	10.8	8.3			
CP1734-S4-W	10.0	8.7			
CP1734-T2-W	10.1	8.3			
CP1734-T3-W	10.6	8.6			
CP1734-T4-W	10.3	8.8			

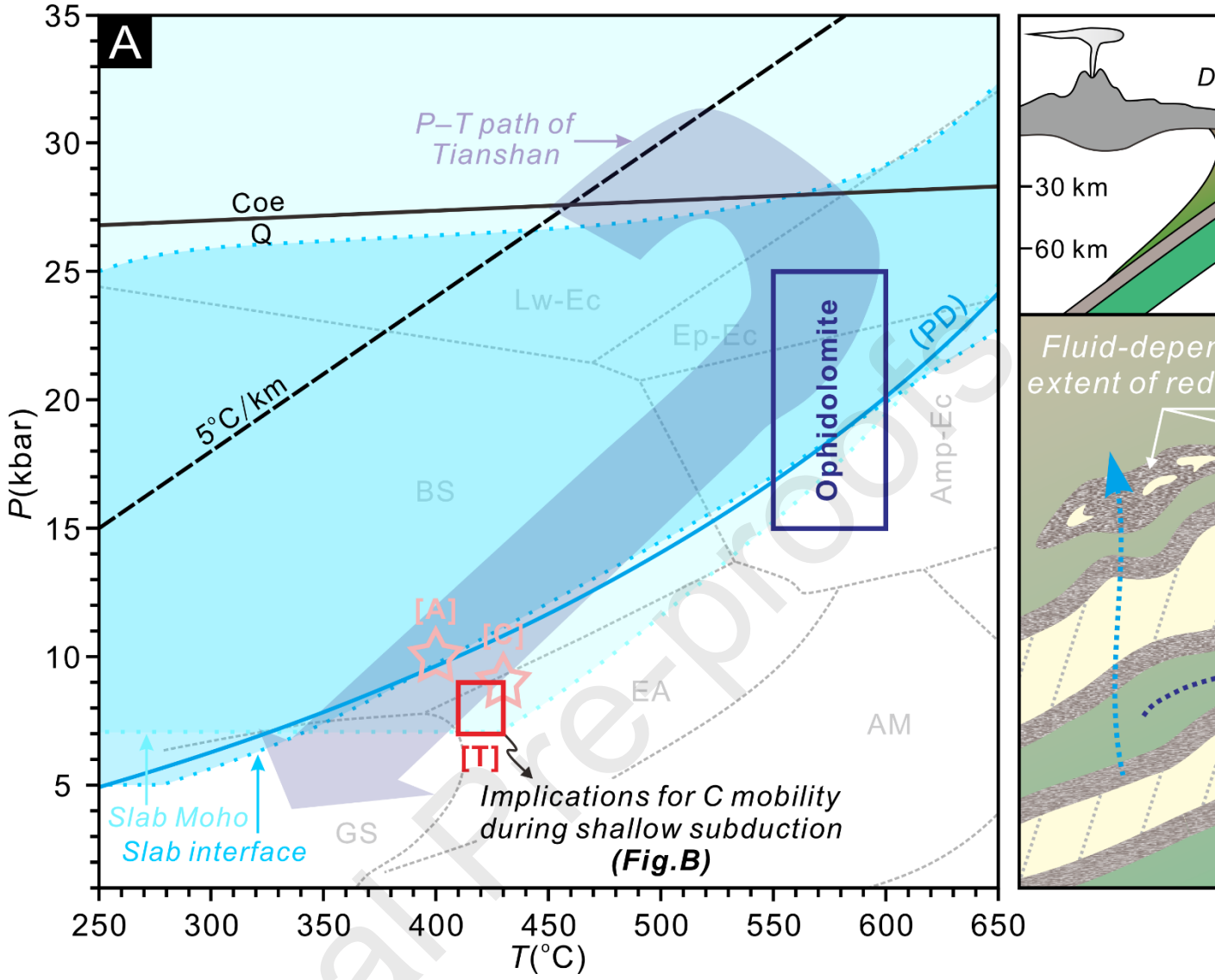

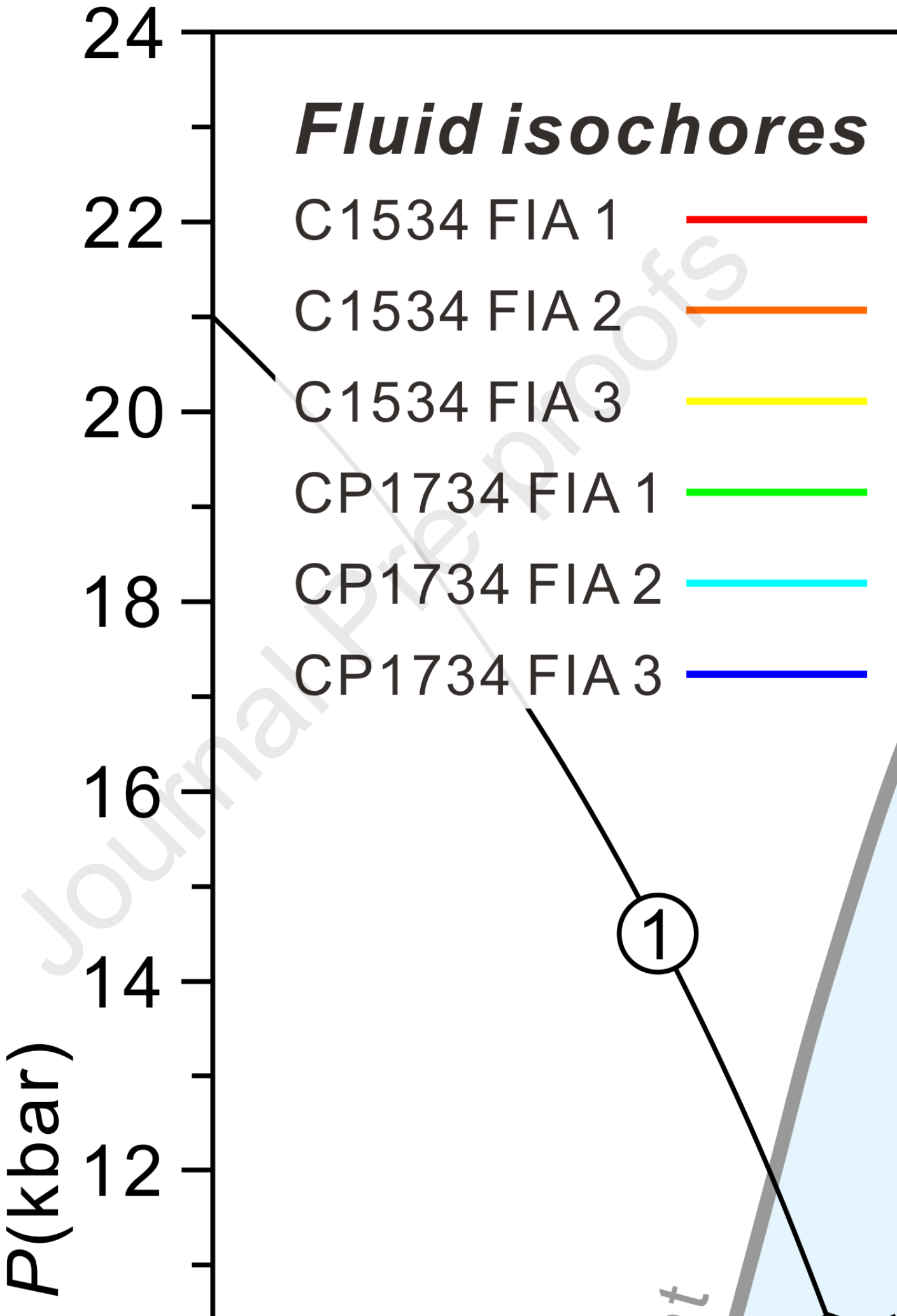

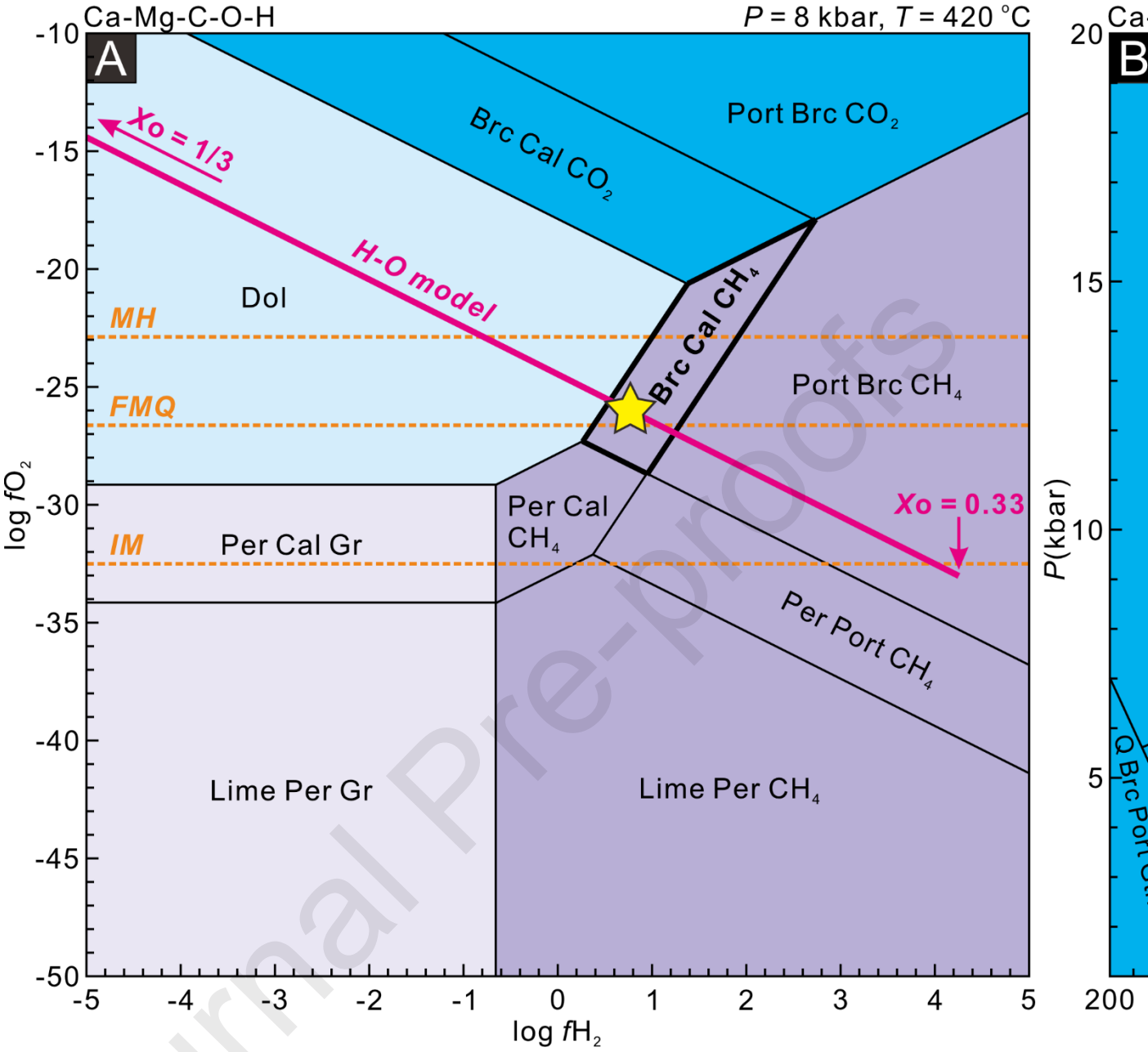

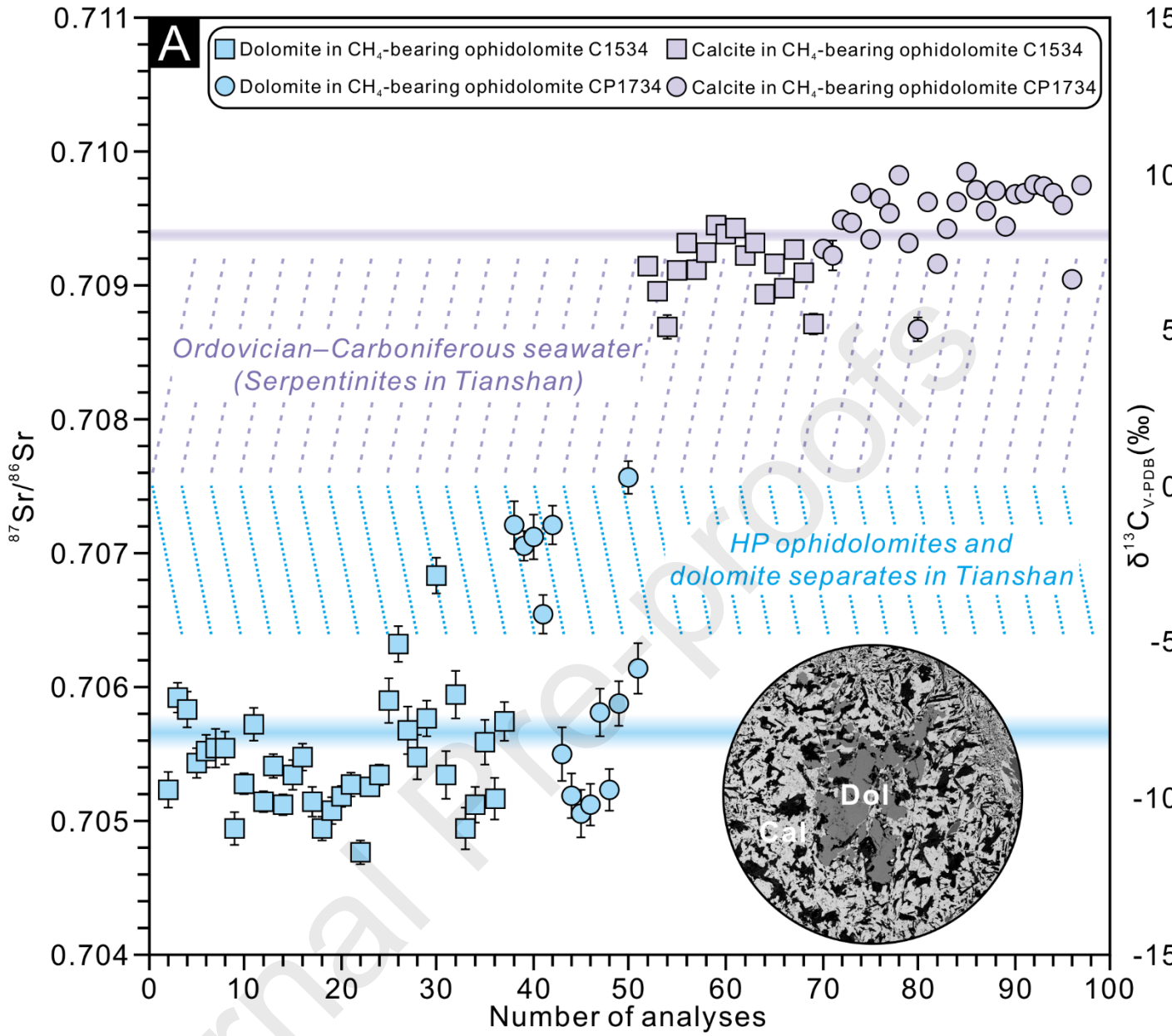

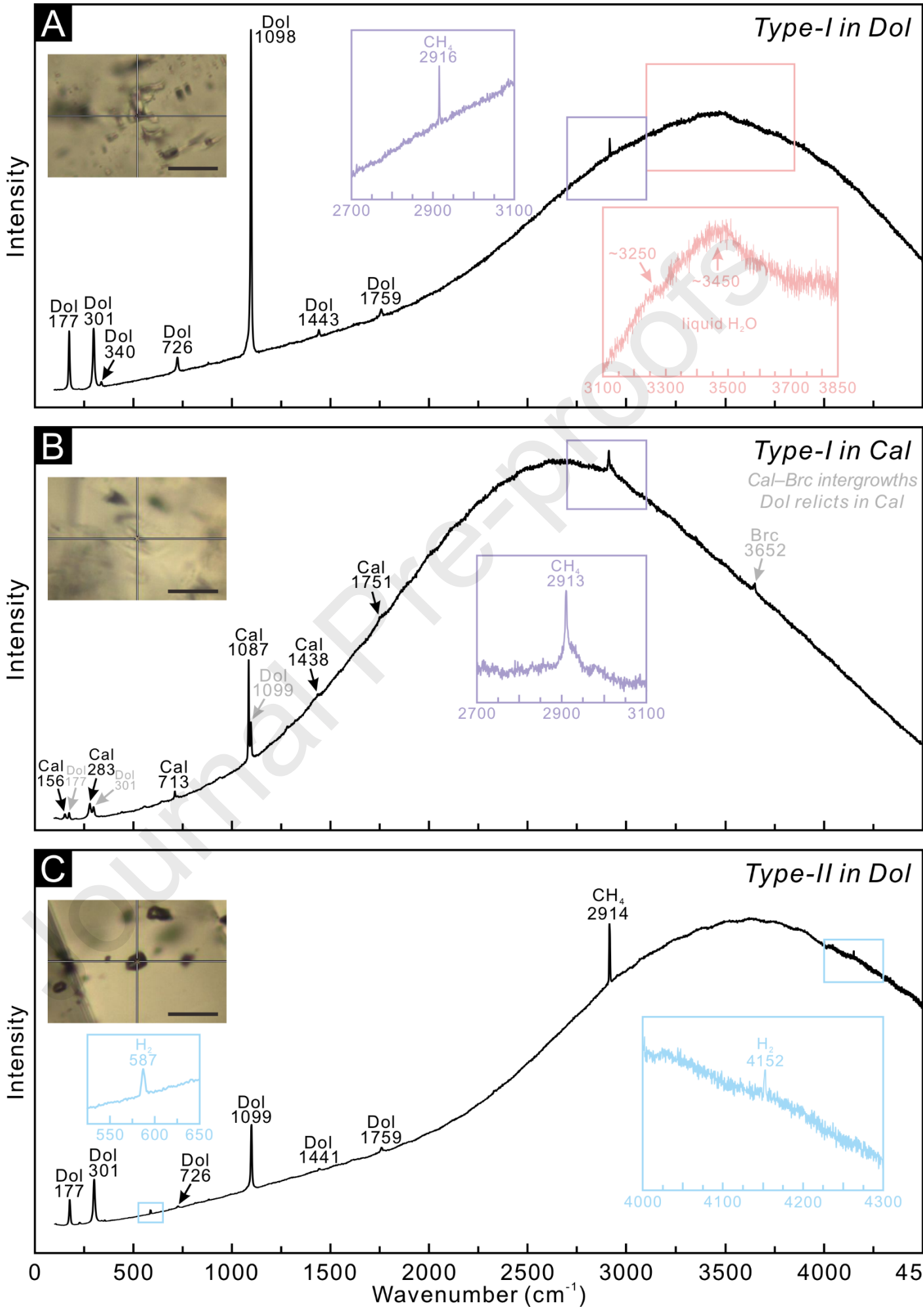

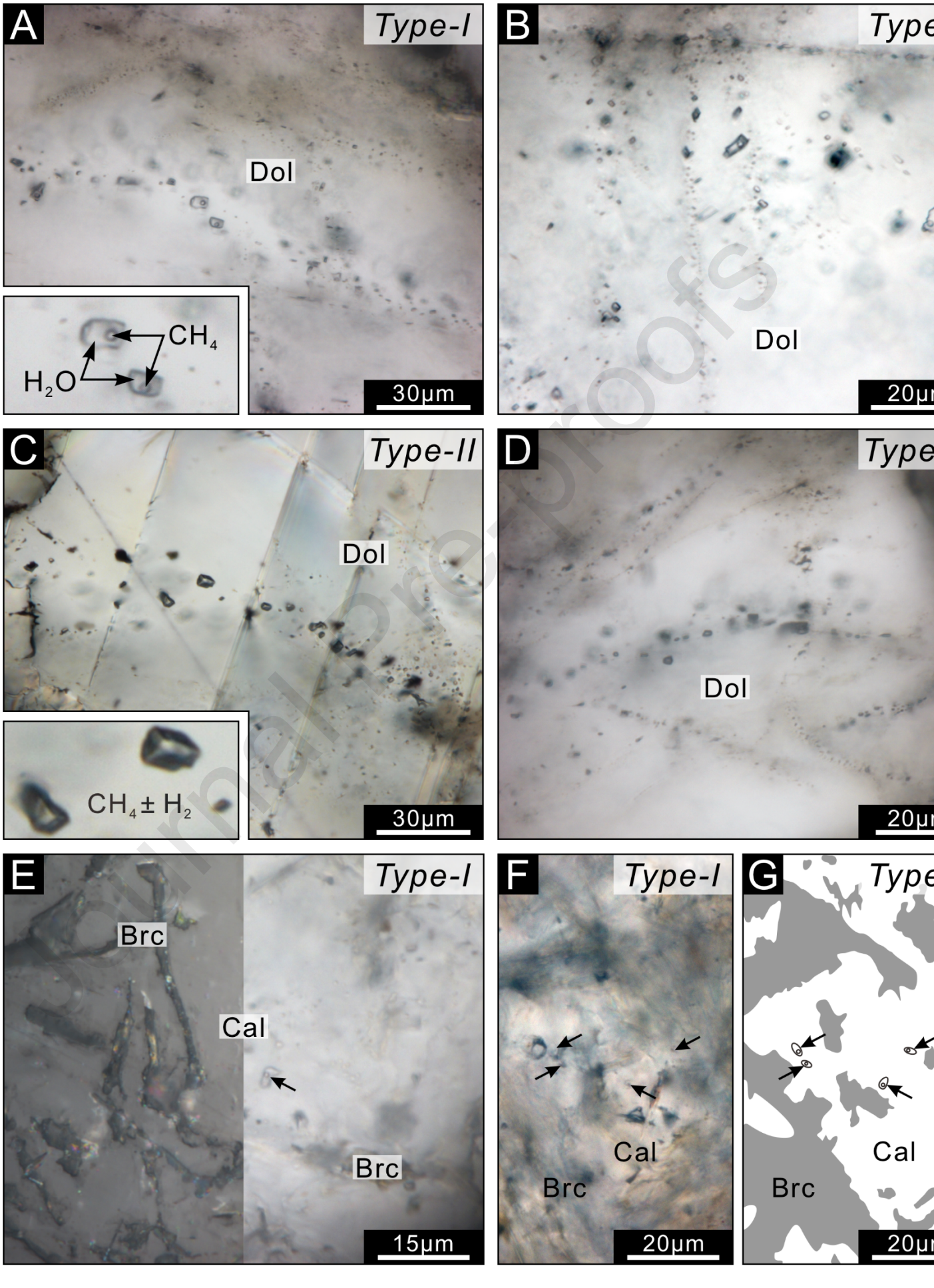

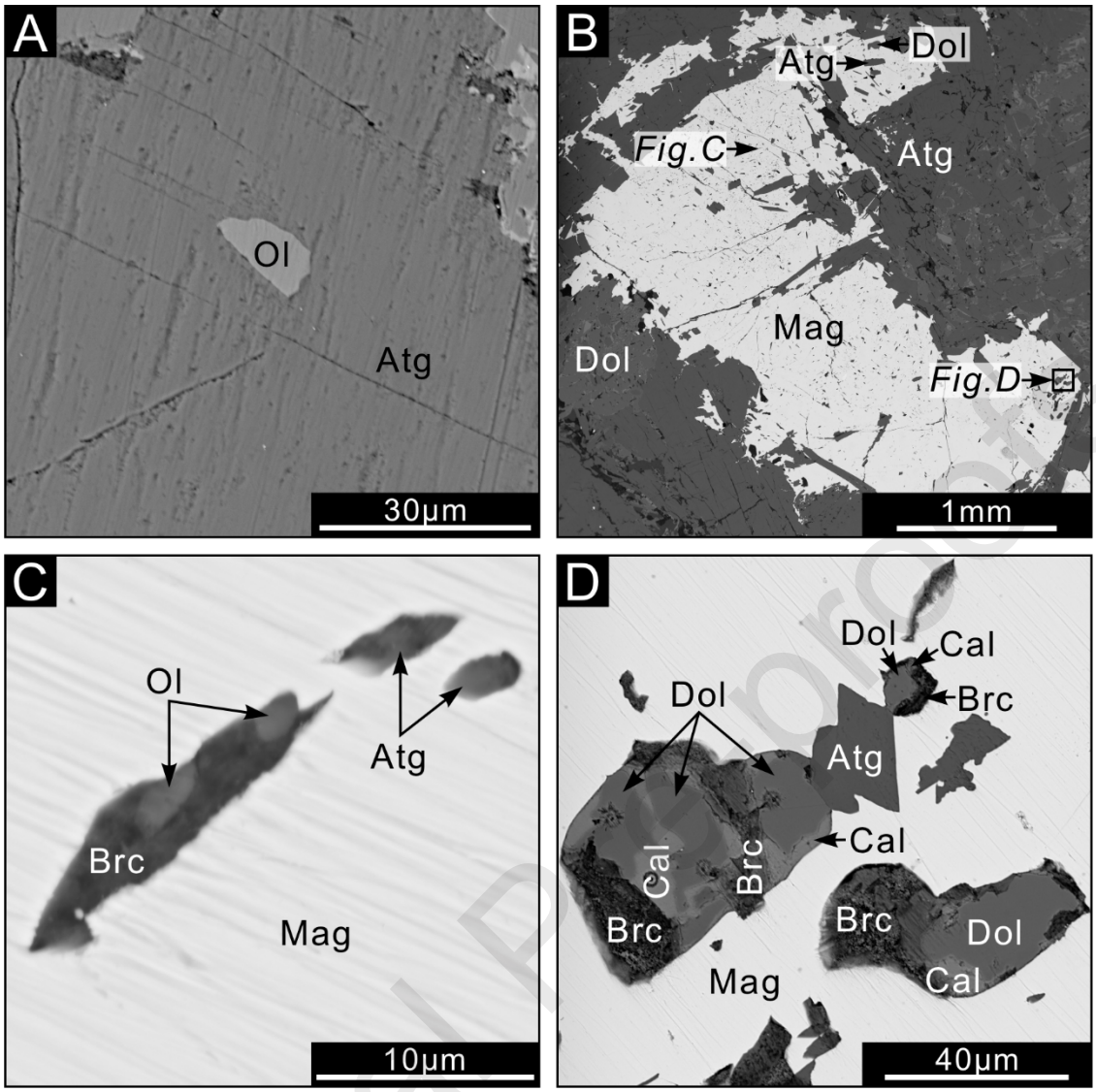

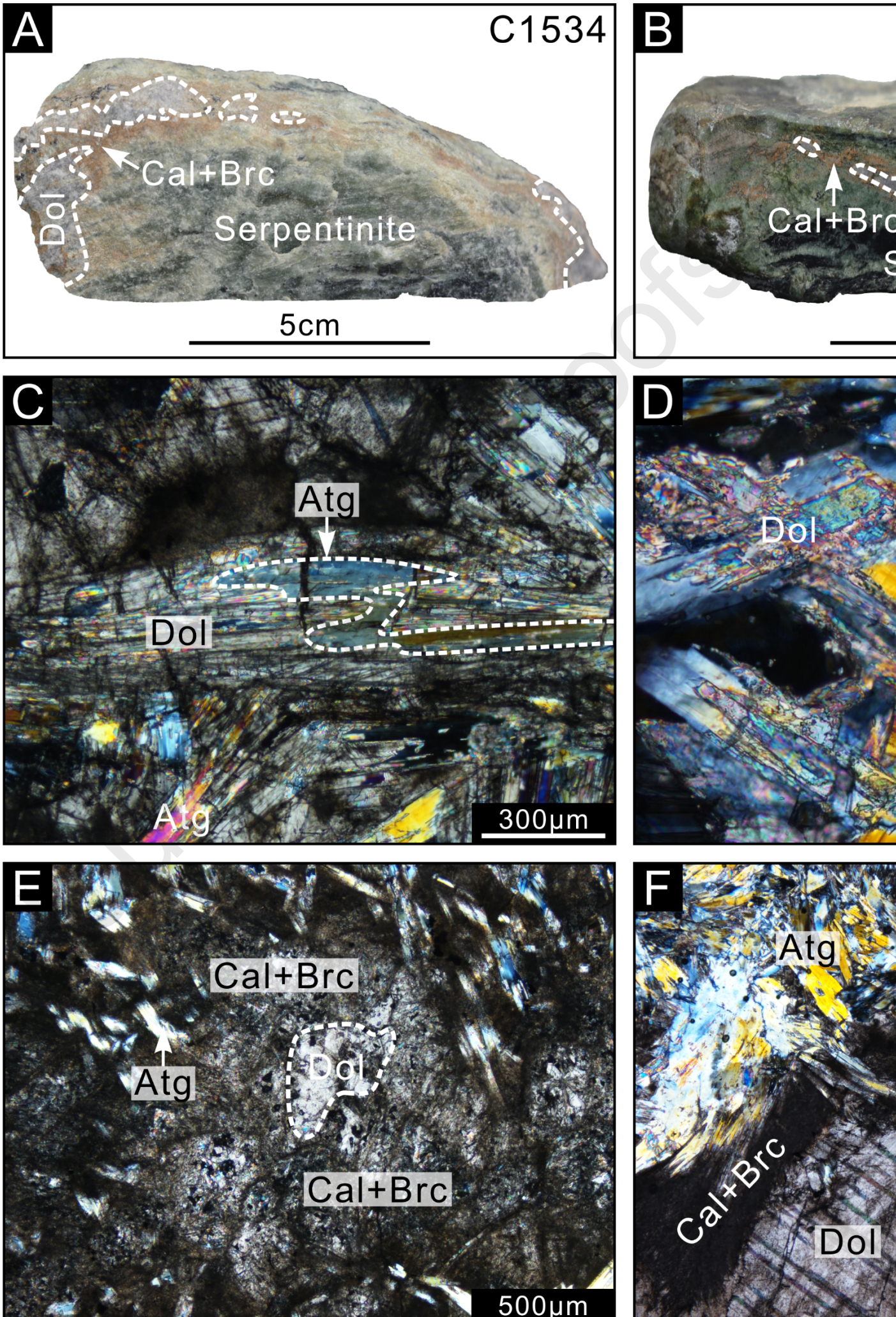
A
C1534
Cal+Brc
Dol
Serpentinite
5cm
B
Cal+Brc
C
Atg
Dol
Atg
300μm
D
Dol
E
Cal+Brc
Atg
Dol
Cal+Brc
500μm
F
Atg
Cal+Brc
Dol